LIGHT WEIGHT and HIGH STRENGTH MATERIALS MADE of RECYCLED STEEL and ALUMINUM

Thomas Nounezi

Thesis submitted to the

Faculty of Graduate and Postdoctoral Studies

In partial fulfillment of the requirements for the degree of

MASTER OF APPLIED SCIENCE

In Mechanical Engineering

Ottawa-Carleton Institute for Mechanical and Aerospace Engineering

Faculty of Graduate and Postdoctoral Studies (FGPS)

University of Ottawa

Ottawa, Canada

January 2012

ABSTRACT

Recycling has proven not only to address today's economical, environmental and social issues, but also to be imperative for the sustainability of human technology. The current thesis has investigated the feasibility of a new philosophy for Recycling (Alloying-Recycling) using steel 1020 and aluminum 6061T6. The study was limited to the metallurgical aspects only and has highlighted the potential of recycled alloys made of recycled aluminum and steel to exhibit substantially increased wear resistance and strength-to-weight ratio as compared to initial primary materials. Three alloy-mixtures are considered: TN3 (5wt% 1020 +95wt% 6061T6); TN5 (0.7wt% 1020 + 99.3wt% 6061T6); and TN4 (10wt% 6061T6 + 90wt% 1020). A Tucker induction power supply system (3kW; 135-400 kHz) is used to melt the alloy mixtures for casting in graphite crucibles. Heat treatment of the cast samples is done using a radiation box furnace. Microscopy, Vickers hardness and pin-on-disc abrasive wear tests are performed.

Casting destroyed the initial microstructures of the alloys leading to a hardness reduction in the as-cast and solution heat-treated aluminum rich samples to 60 Hv from 140 Hv. Ageing slightly increased the hardness of the cast samples and provided a wear resistance two times higher than that of the initial 6061T6 material. On the steel rich side, the hardness of the as-cast TN4 was 480 Hv, which is more than twice as high as the initial hardness of steel 1020 of 202 Hv; this hints to strong internal and residual stress, probably martensite formation during fast cooling following casting. Solution heat treatment lowered the hardness to the original value of steel 1020, but provided about ten (10) times higher wear resistance; this suggests higher ductility and toughness of normalised TN4 as compared to 1020. In addition, TN4 exhibits about 25% weight reduction as compared to 1020.

The actual recycling process and the effect of non-metallic impurities shall be investigated in future works. Also, the casting and heat treatment processes need to be improved.

ACKNOWLEDGEMENT

Accomplishing a task cannot be meaningfully achieved without the support and assistance of our creator and people of substance.

First, to God almighty be all glory for his grace and enablement throughout this programme.

I will also not hesitate to express my profound gratitude to the Ministry of Secondary Education of Cameroon, the body that gave approval for me to proceed on the program as well as providing part funding for the cause.

I am highly indebted to my supervisor, Dr. Michel Nganbe, for his endless and tireless support and efforts to see me through. Without his help, this work could not have been achieved.

I will also not forget the Faculty of Graduate and Post Doctorate Studies (FGPS) staff, and members of the Mechanical Engineering Department at the University of Ottawa who provided all forms of possible support and better working environments. In particular, I thank the Mechanical Engineering workshop staff for their support and understanding.

To the Financial Aid and CUPE of the University of Ottawa, I say a big thank you for their help during critical periods.

To my wonderful friends, parents, sisters and brothers, I say thank you for their inspiration and devotion.

Lastly, to my lovely wife Blanche Nounezi, my sons Nelson, Martial, Phanuel and daughter Lea Nounezi, I am more than grateful for their unflinching love, care, inspiration and devotion, even though, they are far away.

TABLE OF CONTENT

LIST OF FIGURES

LIST OF TABLES

LIST OF SYMBOLS

Symbol (unit)	Definition
αFe	Single phase solid solution iron base in iron-aluminum system
β	Constant dependent on the solute atoms
γ_{wof} (J/m^2)	Work of fracture
$\Delta\tau$	Stress needed to overcome solid solution dislocation effect
ΔG	Free energy
ϵ_a	Lattice distortion term
ϵ_G	Term that capture local modulus change
η	Current efficiency
μ	Magnetic permeability
ρ	Resistivity
$\sigma(\frac{w}{m^2}.K^4)$	Stefan- Boltzmann constant
τ	Critical shear stress
a and b	Ratio atoms or moles of metal and Oxygen in the reaction
A_1, A_2	Molar mass of element 1 and 2
A_s(m^2)	Cross sectional area of the sleeve
B	Magnitude of the Burger's vector
C (J/kg.^{o}C)	Specific heat of the metal
d (m)	Penetration depth
E	Emissivity of the work piece surface
E (volt)	Voltage
E(GPa)	The Young's modulus
G	Shear modulus
Hv	Vickers' number for hardness
I (A)	Intensity of the current
I_C (A)	Intensity of current in the heating coil
K	Equilibrium constant
K_{R_C}	Resistance factor as a function of electrical path applied to R_{eq}
K_{S_2}	Resistance factor f (Air gab, shortness, turns spacing factor) applied to
K and *n*	Time independent constants in Avrami equation
K_{I_C} (MPa-m$^{1/2}$)	Value of the fracture toughness
$d\emptyset/dt$	Change in magnetic flux (Wb/second)

M	Oxidized metal
$\overline{M_i}a$	Mean mass of wear test sample i of material a
N	Number of coil's turns
N(rotations/min)	Circular speed
O_2	Mol of oxygen
PG	Power loss through Joule's effect in the graphite crucible
P	Total power needed from the AC source
$P1$	Power lost through Joule's effect
P_{rad}	Power lost through radiation
P_{conv}	Power lost through convection
P_{coil}	Power lost in the coil through Joule's effect
$R_{eq}(\Omega)$	Equivalent resistance to the work piece placed in series with coil
R	Perfect gas constant
Ω	Resistance
r(m)	Distance from the disc centre to the position of the sample
$r_{solvent}$, r_{solute} (nm)	Atomic radii of solvent and solute
T (Kelvin)	Absolute temperature
TS(Mpa)	Tensile Strength
t (minutes)	Wearing duration
t0.5	Duration for transformation for half of the mass
V(m/s)	Wearing speed
W	Total weight to be heated per unit time
Y	Time progression of the transformation between phases

1 MOTIVATION AND INTRODUCTION

1.1 Motivation

Growing quantities of spare parts from cars and workshops have become an environmental, social and economical issue, particularly in developing countries where recycling is not well established. On the economical point of view, it is known that 20 times more energy is required to refine natural aluminum from ore than from recycled aluminum [1]. For steel processing from ore, 4 times more energy is required than for recycled steel [1, 5]. In addition, mines are being drained out leading to exhaustions of natural resources. This can be very well understood in the case of aluminum for which one ton of Al is produced from four to six tons of bauxite [2]. Therefore, continuous mining alone is clearly an unsustainable path for material supply and technology as a whole. Recycling has been providing some answers to the above issues for decades, along with its attractive advantages and outcomes. However, there are substantial remaining limitations and issues to address. For example, though recycling processing is close to being standard in developed countries, it is still practically absent in developing nations. It is also known that recycled products in most cases exhibit poor properties and performance compared to their primary material counterparts due to the relatively high level of impurities they generally embody. For instance, Aluminum 6061 is one of the most used aluminum alloys and steel 1020 is a mass produced low alloy steel. After recycling the two materials separately, it is well known that they only qualify as much lower grade materials [1] as compared to primary aluminum 6061T6 and steel 1020 due to impurities and/or contaminants [11,12,13].

A different approach could be taken when comparing the different but complementary properties of aluminum alloys, which are lighter but softer, and steels that are heavier but stronger. In this

approach, new types of alloys could be produced that tolerate impurities better than primary materials and eventually yield improved properties. For instance, Al-Fe based alloys made of recycled aluminum alloys and steels could combine the lightweight of aluminum with the high strength of steels to provide a better strength- or stiffness-to-weight ratio, which is one of the top criteria in modern design and construction. In fact, manufacturers have been using high cost primary materials such as titanium and composites in order to achieve this requirement up to now.

1.2 Introduction

1.2.1 Background of standard recycling

Recycled materials can present a substantial cost advantage compared to primary alloys manufactured from newly processed ore, provided the costs of collecting, sorting, refining and reprocessing are sufficiently low. For instance, one of the processes for virgin steel production includes mining, crushing, cleaning, separation and sorting, melting in a blast furnace, conversion in a basic oxygen furnace (BOF) for pre-treatment to remove contaminants such as sulphur, phosphorus and silicon. With respect to virgin aluminum production, one of the most used processes includes bauxite ore mining, alumina production through Bayer process, carbon anode production, aluminum smelting through electrolytic reduction, and ingot casting. In contrast, recycling processes of both aluminum and steel include collection, transportation, sorting, refining, and reprocessing [3].

Energy consumption is the major cost factor of industrial production; in the United States it has been estimated that approximately one-half of the energy consumed by manufacturing industries goes to producing and fabricating materials [1]. Therefore, it is clear that substantial cost savings

can be achieved through metal recycling since recycled aluminum based products require 95% less energy, and steel based ones require up to 74% less energy than virgin materials production from ores [1, 4, 5]. In addition to the cost advantage, metal recycling contributes to solving environmental issues such as excessive mining, gas emission and waste management. Recycled metals are made from scrap collected from various sources and can therefore contain substantial impurities. The less the scrap needs to be refined, the lower their overall re-processing costs. Reprocessing aluminum for aluminum and steel for steel, a practice known as closed loop recycling [5] is an attempt to re-produce materials that are identical to original virgin materials. This means featuring identical chemical composition, microstructure and properties, which requires more extensive refining than producing new classes of materials made by mixing different primary alloys. Therefore, it is hypothesised in the present work that the new alloys with features different to those of primary materials may present a cost advantage. In addition, they could be designed to combine different complementary properties such as the low density of aluminum alloys and the high strength or stiffness of steels. In fact, such new Al-Fe based alloys may be appropriate for modern applications requiring high strength- or stiffness to weight ratios.

1.2.2 The New Philosophy for Recycling

The current thesis does not address the standard recycling procedure of collecting, sorting and refining of recycled scrap, which is well documented in previous literature and of which remaining issues are left for future research work. In addition, the thesis simply focuses on metallurgical aspects of a new philosophy for recycling (Alloying-Recycling) applied to novel Al-Fe based alloys and has the following as objectives:

- To investigate induction heating and melting of existing aluminium 6061T6 and steel 1020.
- To study the effect of heat treatments on microstructure and mechanical properties.
- To investigate resulting microstructures.
- To investigate the resulting mechanical properties including hardness and wear resistance.
- To compare the properties of the newly produced Al-Fe based mixture alloys with those of the primary aluminum 6061 T6 and steel 1020.

The following flow chart Figure 1.1 illustrates the New Philosophy, alloying-recycling for Aluminum/Steel from which three compositions of aluminum 6061T6 and steel alloy 1020 are investigated in the present work. It is known that primary aluminum and steel result from primary processing and are used to build structures for specific applications. These structures are put in use during their service-life and end up as waste. The standard recycling turns this waste into recycled steel or aluminum in a close-loop process as can be seen in Figure 1.1, attempting to give them similar properties and microstructures as their primary counterparts. As seen in motivation section, recycled products are cheaper thus will provide affordable structures; they contain impurities that could form strengtheners like inclusions and precipitates. Knowing their appealing properties, applying this philosophy to aluminum and to steel could lead to an alloy that combine the ductility, light weight, corrosion resistance of the first and high strength of the latter. Following the maximum solubility displayed by the iron-aluminum phase diagram, the new philosophy intends to add a certain percentage of recycled steel in aluminum as shows the thin green arrow “a” to have aluminum rich alloy; and to obtain steel-rich alloy, a certain

percentage of recycled aluminum in steel as seen thin blue arrow “b”. The resulting alloys either heat-treated or not will be characterized to assess the weight reduction and increase in strength.

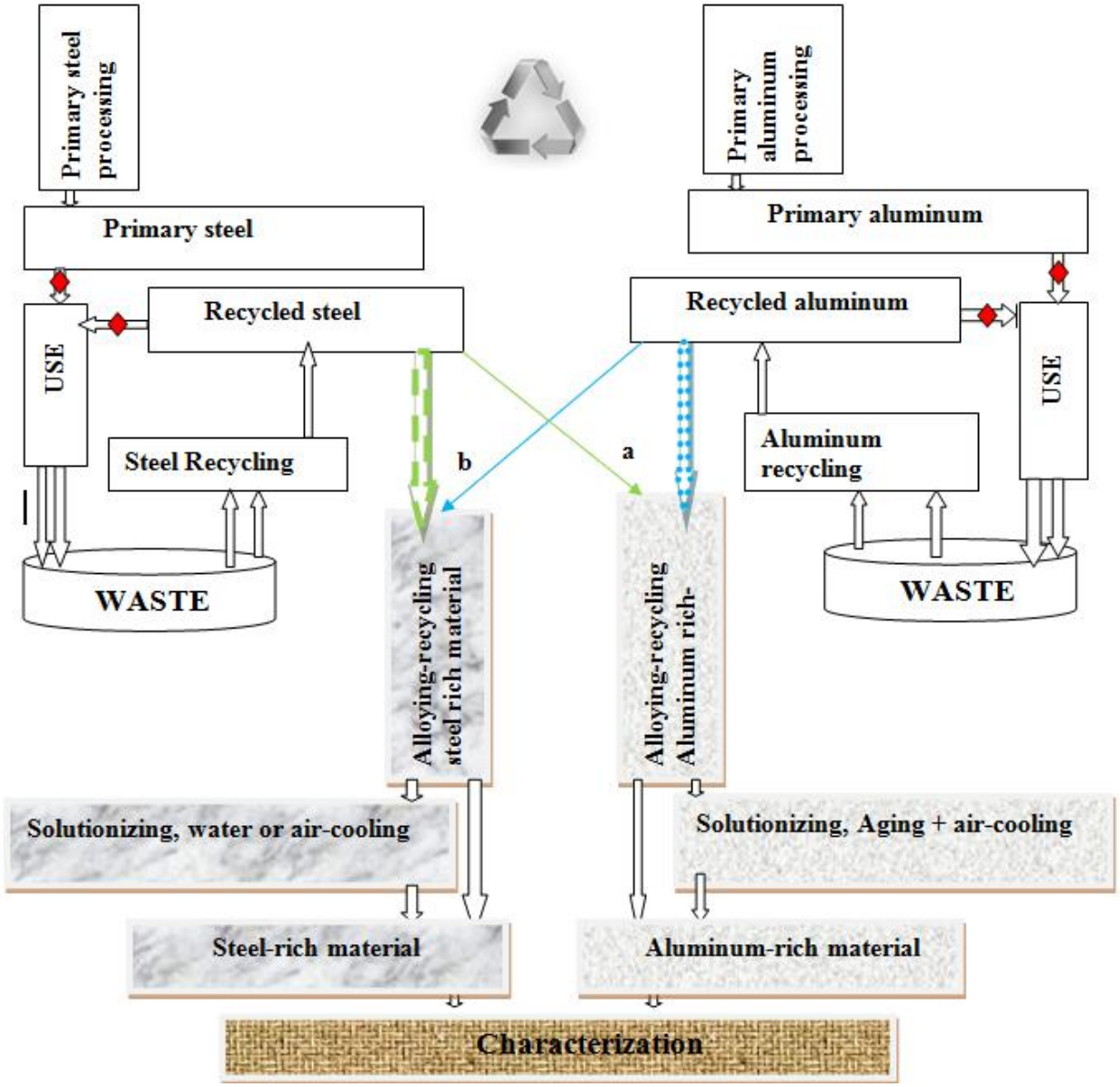

Figure 1.1: Flow chart illustrating the New Philosophy, Alloying-Recycling for Aluminum/Steel

2 LITERATURE REVIEW

2.1 Recycling

2.1.1 Theories that govern recycling

The recycling process can be subdivided into a phase of recovery and removal of hazardous contaminants and a metallurgy phase. The Pourbaix diagram helps to understand the separation of ferrous scraps prior to metallurgical reprocessing. It describes the thermodynamic stability of metals that have oxidised components as a function of the pH of the aqueous solution. Thermodynamic rules state that in chemical reactions, if the free energy of the reactants is higher than that of the products, a reaction will occur. The free energy change for oxidation reactions is given by:

$$\Delta G^o - RTlnK \tag{2.1}$$

K is the equilibrium constant. T is the absolute temperature in Kelvin, R is the constant of perfect gas, ΔG^0 is the free energy at initial state. At equilibrium, $\Delta G = 0$ then (2.1) becomes,

$$\Delta G^o = RTlnK \tag{2.2}$$

Based on equation (2.2), the other tool used for material preparation prior to recycling is the Ellingham diagram, which plots the temperature T against ΔG^0 [6]. The Ellingham diagram helps to determine the boiling and melting points and at a given temperature, the partial pressure of oxygen needed to oxidise the elements, and to reduce the metal oxide. The melting point, the boiling point and the constituent elements differ for aluminum and steel, therefore their recycling processes are also different.

2.1.2 Aluminum recycling

Recycling turning chips of Al via cold pressing and melting with salt flux

The following operations are used for aluminum scrap recycling: direct conversion of chips into a compacted form, powder metallurgy, extrusion and melting using protective salt [8]. Amini showed that weight loss could be minimised by melting aluminum after cold pressing the scrap and melting it with salt flux**.** As seen in the following diagram, cold compaction at up to 900 MPa compaction pressure improves the recyclability ratio up to 70%. No significant change occurs beyond 900 MPa. In the target range, high compaction reduces the metal surface in contact with air and thus reduces oxidation.

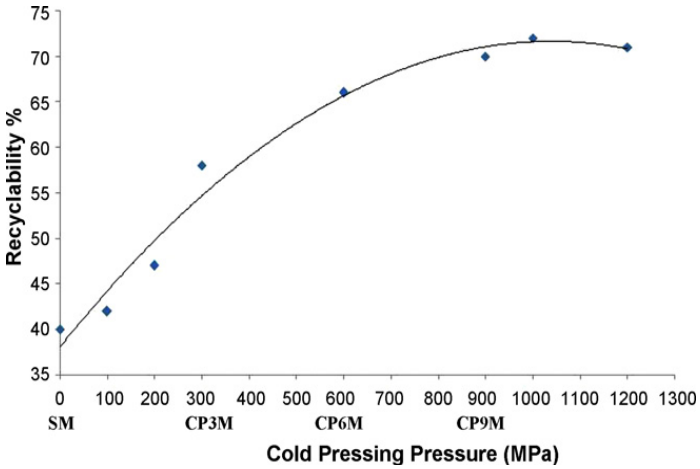

Figure 2.1: Recyclability versus cold pressure in aluminum recycling [8]

With the above methods, the maximum recyclability ratio achieved is around 70%, which means 30% loss even at high compaction pressure. This implies the need for additional processes such as the use of protective salt flux to eliminate oxidation [8]. To establish optimal melting conditions and ensure the highest metal recovery rate, the steps to follow include swarf conditioning, use of a suitable furnace type (induction melting furnace), use of argon protective atmosphere or vacuum, achieving a high melting temperature. Additional steps can include

allowing the swarf to decant (12h) and decreasing the moisture content, centrifuging the swarf (for 10 min at 400 rpm), and compacting it into briquettes using high pressure compaction. The swarf briquettes can then be introduced into already molten liquid aluminum in order to prevent briquette oxidation, and the melt is usually degassed. Grain refinement can be achieved after degassing using different additions of Al-Ti-B master alloys [8].

Influence of the melting furnace and atmosphere on aluminum recovery rate

Melting with induction furnaces leads to higher recovery rates (around 85 %) as observed by Verran and Kurzawa (2008) [9]; the interaction of current in the melt with the electromagnetic field produces a stirring motion that leads to the destruction of the oxide film, thus increasing the volume of molten aluminum that is recovered [9]. In addition to oxygen, exposure to atmospheric environment can also lead to hydrogen absorption by the liquid metal. Hydrogen has a higher solubility in liquid aluminum than in solid aluminum [24], and its solubility decreases rapidly during cooling causing the excess hydrogen to precipitate in molecular form, resulting in the formation of primary and/or secondary voids. Therefore, the use of protective argon or nitrogen atmosphere during melting is a crucial factor as it decreases the probability of hydrogen and oxygen pick up by the molten aluminum thereby increasing the aluminum recovery rate [10].

2.1.3 Steel recycling

Effects of contaminants and alloying elements

Little research literature is available on the main factors influencing the metallurgical properties of recycled steel. The major technical problems resulting from the use of scrap are caused by contaminants that cannot be removed in steelmaking and adversely affect the quality of the recycled steel. Some elements can also cause furnace damage; in particular, lead can penetrate the furnace bottom, and the most important contaminants present in scrap are copper and tin. Automotive scrap contains copper, either from the electrical systems, or from other copper-bearing parts in the form of brass. Bearings and solder introduce tin and lead; tin would also be present if tin cans were recycled without prior de-tinning [11]. How harmful impurities are, depends upon the intended application of the steel. Impurities in reinforcement bars, for example, would make them entirely unsuitable for automobile body sheet. The average contamination increases as steel is converted into consumer and other products. In addition, traces of phosphorus in oil do not slag out during reheating, but instead accumulate in the steel resulting in poor product quality. Some of the technical criteria for recyclable swarf are that it shall contain 0.03% or less by weight of phosphorus and must be low in oil content (approximately < five 5wt %). Knowing these technical problems, chemical specifications implemented in the recycling processes are primarily intended to limit the concentration of contaminants [12]. The following Table 2.1 shows four groups of alloying elements based on their behaviour during recycling.

Table 2.1: Behaviour of alloy elements and impurities in steel making [14]

Behaviour	Elements and impurities
Group 1 Elements almost completely taken up by the slag	Silicon, aluminum, titanium, zirconium, boron, vanadium
Group 2 Elements distributed between the slag and metal	Manganese, phosphorus, sulphur, chromium
Group 3 Elements remaining almost completely in solution in the steel	Copper, nickel, molybdenum, cobalt, tungsten, probably arsenic and antimony
Group 4 Elements eliminated from slag and metal	Zinc, cadmium, lead

Alloy elements in Group 3, such as nickel and molybdenum, are essential constituents of certain alloy steels, but are undesirable if present in other steels because they cause unpredictable responses to heat treatment [12, 13].

Scrap in steel making Processes

Recycling steel from grinding swarf is a complete recovery recycling procedure that involves several steps, such as oil and phosphorus additive removal, drying, metallic/non-metallic separation, and downstream treatment. Removing oil and phosphorous from the solid is the most difficult and important step [16]. Hong focused his research on this specific aspect and suggested two processes for swarf cleaning, aqueous surfactant washing and SCCO2 (super critical carbon dioxide) extraction. Aqueous washing is a low-pressure process involving the use of expensive specialty surfactant packages. Recovery of water and surfactant is an important consideration, which affects the practicality of this procedure. SCCO2 extraction utilizes the increased solvating power of CO_2 at temperatures and pressures above its critical point (Tc=31.1^{o}C, Pc=78.0 atm) [16]. The most notable desirable features of this technique are that

CO_2 leaves no residue in the processed solid, and the isolation and recovery of solute and solvent for reuse can be fulfilled upon a simple mechanical expansion to atmospheric pressure [16].

2.2 Alloying Aluminum and steel through casting

Due to the huge technological importance of steel (high strength and low cost) and aluminum alloys (lightweight, good ductility and corrosion resistance), manufacturing processes, microstructures and behaviour of Al-Fe alloys have been the focus of a multitude of scientific investigations in the past decades. Based on the emf Standard and galvanic series, galvanic corrosion can be expected in some cases due to the large electrochemical potential difference of 1.22 volts between iron and aluminum [38]. Processing methods suggested for alloying Al and Fe include powder metallurgy and casting among others.

2.2.1 Solubility

The solubility is the ability of an element (solute atoms) to dissolve into another (solvent) to form a solid solution alloy with the same crystal structure as the base material (solvent). The solubility limit is the maximum amount of solute atoms that can dissolve into a given solvent to form a solid solution alloy. In crystalline structures, the solute element can either take the place of a host atom of the matrix within the lattice (substitutional position) or can locate in a space between the lattice points (interstitial position).

Beyond the solubility limit, there is saturation and instead of having a solid solution that is a homogeneous single phase, new phases (precipitates) form to accommodate the excess solute atoms. For substantial solubility in substitutional solid solutions to be possible, the following Hume-Rothery rules should be fulfilled.

- The atomic radii of the solute and solvent atoms must differ by no more than 15%:

$$\%\text{difference} = \left(\frac{(r_{solute} - r_{solvent})}{r_{solvent}}\right) * 100 \ \leq 15\% \quad (2.3)$$

- The crystal structure of solute and solvent must match.
- Solvent and solute atoms shall have the same valence; metals with lower valence will tend to dissolve in metals with higher valence.
- Solute and solvent atoms should have similar electro negativity; if the electro negativity difference is too great, the metals tend to form intermetallic compounds instead of solid solutions.

For interstitial solid solutions, the Hume-Rothery rules are:

- Solute atoms must be smaller than the interstitial sites in the solvent lattice.
- The solute and solvent atoms should have similar electro negativity.

2.2.2 Solubility of aluminum and steel

At room temperature, the crystal structure for aluminum is FCC (Face Centered Cubic) while that of iron is BCC (Body Centered Cubic). While aluminum maintains the FCC crystal structure until melting, the BCC structure of iron allotropically transforms into FCC above 912^{o}C, then back into BCC above 1394^{o}C prior to melting [20]. The atom radius of aluminum is 0.1431nm and that of steel is 0.1241nm [20]. The different crystal structures of aluminum and iron at room temperature combined with an atomic radius difference of 13.27% close to 15% suggests a limited solubility of the two elements in each other as can be seen in Aluminum-iron phase diagram in Figure 2.2.

2.3 Phases and phase diagrams

A phase is defined as a physically distinct and homogeneous volume in a material. Each phase shows its own specific characteristics and properties even when it has a chemical composition similar to that of their neighbouring volume.

In general, two-phase alloys are stronger but less ductile than their single-phase counterparts [20]. Equilibrium phase diagrams help to predict phases that are stable at equilibrium which, at given chemical composition, temperature and pressure, is achieved by sufficiently slow cooling or heating. Phase diagrams for materials and manufacturing applications are developed for atmospheric pressure, which means only the chemical composition and the temperature are considered varying parameters. Non-equilibrium rapid cooling or heating produces meta-stable phases and alloys that easily change their structure at temperatures at which diffusion allows a re-arrangement of atoms into a stable microstructure, as predicted by phase diagrams. The Al-Fe phase diagram (Figure 2.2) shows a solubility of Al in Fe of up to ~ 12wt % (~20at %), while practically no iron can be dissolved in aluminum. The melting temperature of Al-Fe alloys decreases nearly continuously with Al concentration from 1538°C (melting point of pure iron) to 660°C (melting point of pure aluminum).

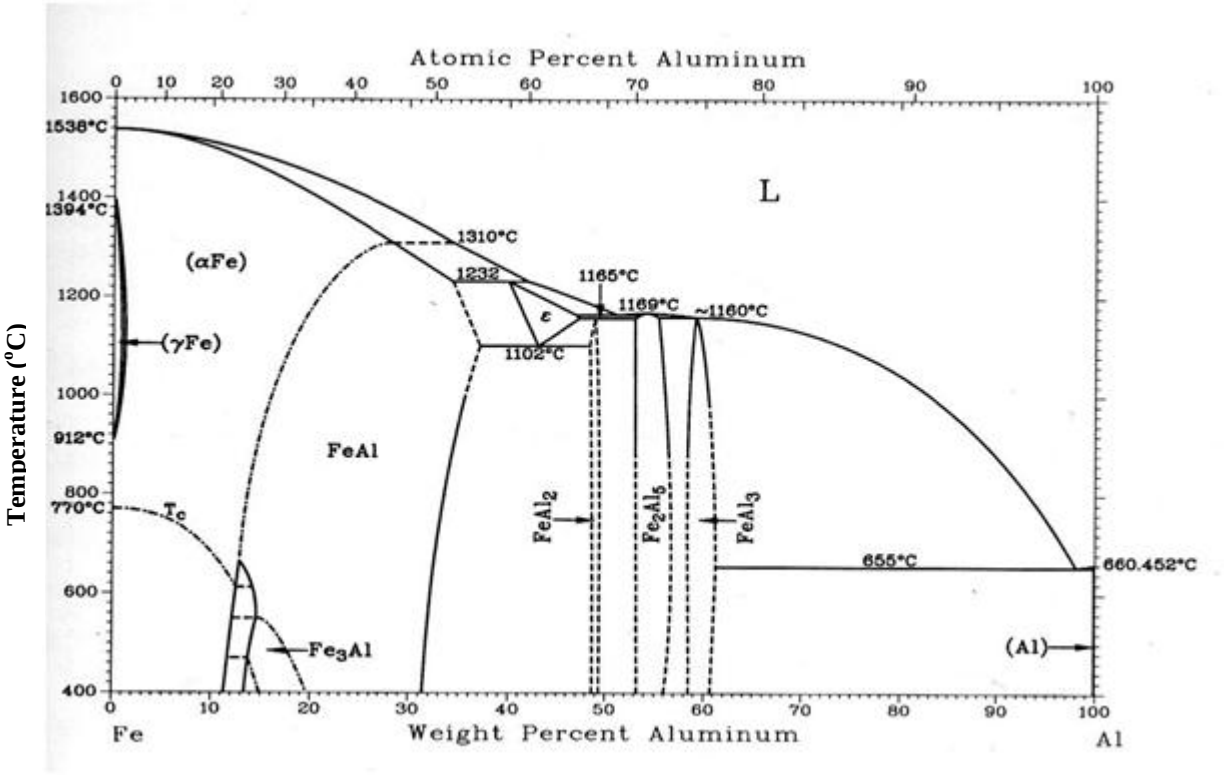

Figure 2.2: The aluminum-iron phase diagram [17]

In determining the number of phases, their compositions and mass fractions, the phase-field rule specifies that at constant temperature and pressure, the number of phases in adjacent fields in a multi-phase component diagram must differ by one. According to the Le Châtelier theorem, phase transformation in a system occurs in the way to nullify constraints imposed by the change in parameters or conditions. The tie line horizontal rule and the lever rule are used to determine phase compositions and fractions in a multi-phase region, respectively.

Due to the limited solubility of Al and Fe in each other, Al-Fe alloys are rarely single-phase solid solutions. Instead, they are mostly composed of various types of inter-metallics, of which Table 2.2 summarises the most discussed in literature to date. Inter-metallics are ordered structures also called super-lattices. They result from the ability of the atoms within many alloy phases to arrange themselves into specific configurations. For instance, one type of atoms can

locate at corners of the cubes of an FCC unit cell while the other type of atoms locates at the centre of the cube phases.

Table 2.2: Summary of inter- metallics found in FeAl alloys [15]

Bimetal joint	Al Content (At%)	Structure	Micro hardness (Hv)	Density (g/cm^3)
Fe_3Al	25	Ordered BCC	250-350	6.67
FeAl	50	Ordered BCC	400-520	5.37
Fe_2Al_7	63	Complex BCC	650-680	5
$FeAl_2$	66-66	Complex rhombohedral	1.000-1050	4.36
Fe_2Al_5	69.7-73.2	BCC orthorhombic	1,000-1,100	4.11
$FeAl_3$	74-76	Highly complex monoclinic BCC	820-980	3.95

2.4 Casting aluminum and steel alloys and resulting properties

Conventional casting of iron aluminides has proven to be difficult. Segregations often result in inter-metallics formation that are brittle and can cause micro cracking during cooling or subsequent processing. An added disadvantage is that the grain size of castings is very large in most cases. Therefore, secondary processing is essential for optimizing the microstructure. Generally, changes in temperature and annealing time affect the elongation, yield strength and ultimate strength of the alloys. Increasing the Al content enhances ductility but reduces strength. Increased Fe content can reduce the cooling rate (probably due to the lower heat conductivity of iron as compared to aluminum). High Fe levels result in more Fe-rich inter-metallics particles that can act as nucleation sites for porosity. Also Fe-rich inter-metallics platelets can impede the flow of inter dendritic liquid during feeding, and thus can promote the formation of shrinkage porosity [23, 16, 24]. Particularly, investigations of Al-12Si-1Cu-0.1Mg Alloy showed that

increased Fe contents lead to a significant increase in volume fraction and aspect ratio of Fe-rich inter-metallics. In fact, iron aluminides, specifically Fe_3Al and FeAl, are typically brittle at room temperature, although their predominantly {110} <111> slip systems provide the necessary five independent slip systems.

Overall, higher Fe contents can lead to higher casting defect concentrations and to a more brittle microstructure [25]. However, Fe increases the hardness of Al alloys. The hardness remains constant at about 86 Hv up to 0.6 wt% Fe, then significantly increases to 105 Hv with further increasing Fe content [26]. Grain boundaries in ordered alloys typically have unique structures with high energy. This plays a role in other grain boundary properties such as mobility, segregation and fracture. Grain growth studies of B2 FeAl indicated that grain boundary mobility is fairly high in these ordered microstructures and the grain growth rate was found to decrease with increasing aluminum content [16].

As described up to this point, material separation, recovery and cleaning have been thoroughly investigated and are well described in literature. Therefore, the current thesis focuses on the metallurgical aspect of alloys made of previously manufactured steels and aluminum alloys.

2.4.1 Metallic materials: aluminum alloys and steels

To meet the different requirements of various applications involving aluminum and steel, their respective alloying elements contents can be changed and treatments can be made leading to various aluminum alloy and steel types resulting from various strengthening mechanisms [27]. In solid solution alloys processing, the alloying element diffuses into the matrix and all elements form a solid solution alloy that may be stronger than the solvent. Substitutional solid solution strengthening occurs when the solute atom is large enough that it can replace solvent atoms in

their lattice positions. Interstitial solid solution forms when the solute atom size is at least 50% smaller than the solvent atoms. Solute atoms introduced during solid solution form local stresses that interact with dislocation stress fields, and introduce lattice distortions and modulus effects [27].

2.4.2 Size and modulus effects in solid solution strengthening mechanism

Stresses acting to stop dislocations or to impede the deformation of the structure increase the yield strength of the material. Such stresses cause the attraction or repulsion of dislocations at solute atoms. From the modulus effect concept, it is known that when the modulus of solute atoms differs from that of the host elements, the local energy around the dislocation is changed, increasing the amount of force needed to deform the material. In addition, the difference in lattice parameters of the two components leads to a high stress field around the solute atom that impedes the movement of dislocations and thus deformation. The governing equation of the stress τ needed to overcome solid solution dislocation effects is:

$$\Delta\tau = Gb\epsilon^{\frac{3}{2}}\sqrt{C} \tag{2.4}$$

Where, *C* is the concentration of the solute atoms, *G* is the shear modulus, *b* is the magnitude of the Burger's vector, and ϵ is the lattice strain due to the solute atoms. The lattice strain ϵ is composed of two terms, one describing the lattice distortion and the other the local modulus change [28].

$$|\in| = \in_a - \beta \in_G \tag{2.5}$$

Here, ϵ_a is the lattice distortion term, β a constant dependent on the solute atoms and ϵ_G the term that captures the local modulus change. The lattice distortion term and the local modulus change can be described respectively as

$$\epsilon_a = \frac{\Delta a}{a \Delta c} \qquad \epsilon_G = \frac{\Delta G}{G \Delta C} \tag{2.6a, 2.6b}$$

Where *a*, is the lattice parameter and G is the shear modulus of the host material [28].

2.5 Weight reduction expected from alloying AL 6061T6 and steel 1020

Increasing the strength to weight ratio (lightweight) is one of most prominent requirements in today's engineering structures and equipments, since this is known to reduce both energy consumption and emissions. The relationship between weight and energy is known from dynamics fundamentals, which state that, for a given acceleration, the greater the mass, the higher the force and the kinetic energy for moving or stopping the structure. Therefore, reducing the energy consumption can be easily achieved by reducing weight. One way of achieving weight reduction is by decreasing the density defined as:

$$\rho = \frac{n\,A}{V_C\,N_A} \tag{2.7}$$

where n is the number of atoms in a unit cell, A is the atomic weight, V_c is the volume of a unit cell, and N_A is the Avogadro's number [29].

For binary alloys, the density (ρ_{ave}) and molar mass (A_{ave}) are estimated as:

$$\rho_{ave} = \frac{100}{\frac{C_1}{\rho_1} + \frac{C_2}{\rho_2}} \qquad \rho_{ave} = \frac{C_1' A_1 + C_2' A_2}{\frac{C_1'}{\rho_1} + \frac{C_2'}{\rho_2}} \tag{2.8a, 2.8b}$$

$$A_{ave} = \frac{100}{\frac{C_1'}{A_1} + \frac{C_2'}{A_2}} \qquad A_{ave} = \frac{C_1' A_1 + C_2' A_2}{100} \qquad (2.9a, 2.9b)$$

where C_1, C_2, C_1', C_2', A_1 and A_2 are respectively, the concentrations in weight per cent and atomic per cent, and molar masses of elements 1 and 2 [29].

2.6 Manufacturing

Metals' composition and processing determine the microstructure, which in turn determines the properties and service behaviour of materials [30]. Except for powder metallurgically manufactured alloys, material processing starts with casting, followed by thermal or thermo-mechanical treatments to create the optimal microstructure for a given application. Basic understanding and interpretation of the phase diagram are very useful in selecting compositions and temperatures for the desired phase and properties.

2.6.1 Casting

To reach the required fluidity and fluid flow, the metal to be cast should be heated above its melting point, temperature at which solid atomic bounds are broken. A protective environment is also needed to avoid oxidation. It is well known that melting practices have a direct bearing on the quality of castings [31].

The melting furnaces commonly used in foundries are electric arc furnaces (EAF) with high melting rate, which is suitable for industrial applications; crucible furnaces that could be a source of contamination with oxide inclusions; and cupolas that require major investments. For

their part, induction furnaces are useful in smaller foundries and suitable for laboratory experiments. They also have a strong electromagnetic stirring action during induction heating as well as excellent mixing characteristics for alloying and adding new charges of metal.

2.6.2 Precipitates and impurity issues in steel casts

Precipitates found by Dutcher Daniel [25] in steel include complex aluminum nitride, carboboride, ferrite network, inter-granular sulfides, and semi-continuous borides, all of which are embrittlers in castings. To reduce oxide formation, aluminum or silicon can be added to steel to remove oxygen [32]. This addition causes the dross to float to the top where it can be skimmed off before the metal is poured into the mould. Depending on the amount of gas evolved during solidification, three types of steel ingots can be produced: killed-steel is fully deoxidized and has practically no porosity; semi-killed steel is partially deoxidized; killed steel can also be rimmed. Rimmed-steel generally has low carbon content (less than 0.15%).

2.6.3 Precipitates, impurities and inter-metallics issues in aluminum casts

During reaction between water vapour and the cast, hydrogen is released and diffuses into the metal melt. Oxygen can diffuse into the melt to form oxides (Al_2O_3) if the cast is in contact with air. Another Al_2O_3 source in aluminum melts is aluminum scrap with an oxidized surface, found when scrap is used in the production of recycled aluminum. Turbulences in the melt caused by careless stirring in furnaces and ladles also contribute to an increased oxidation [24]. It has also been found that the presence of Cu, Mg promotes the formation of other phases [33,34]; copper and magnesium lead to the formation of strengthening Al_2Cu and Mg_2Si precipitates [33,35] while Fe promotes the formation of various inter-metallic phases. The most common of

these inter-metallics are Al_5FeSi (needle-like) and Al15 (Mn, Fe3Si2) (angular globules, block-like) [35, 36].

2.6.4 Casting defects and mechanisms of their occurrence

The following irregularities were identified in castings: gas porosity, shrinkage defects, mould material defects, pouring metal defects, and metallurgical defects [37, 38].

- Gas porosity forms within the material as it cools because the liquid material can hold large amounts of dissolved gas and then release it during solidification forming cavities in the final solid [24,39]. This defect may be at the surface or in the interior and may lead to stress concentration or fracture. Drying of the mould to eliminate humidity prior to pouring can reduce the risk of micro-porosity.

- **S**hrinkage defects occur in the form of pipes at the surface, or as closed shrinkage, which is also called shrinkage porosity. Shrinkage defects occur when no liquid is available to compensate for shrinkage as the metal contracts [39, 40]. Expressing the contraction or expansion as a percentage of the casting volume, shrinkage is 7.1% for aluminum, 4% to 5.5% for white iron, and 2.5% to 4% for carbon steel. Shrinkage can cause dimensional changes and sometimes cracking.

- Pouring defects include miss-runs and cold shots and are caused by insufficient quantity of melt, less fluidity, and too narrow cross sections of the mould cavity [39, 40].

- Mould material defects include molten metal run out due to mould flash. In addition, the mould can weaken leading to rat tails (small) or buckles (large) under pressure due to heat [39, 40].

Process specific defects may arise from uneven cooling, molten metal quality, chemical composition and cleanliness [36].

During casting, the melt may carry air mechanically. In addition, in sand moulds there is moisture that at the contact with the melt may lead to water vapour, gas dissociation and generation of hydrogen (H_2)[24]. Reactions with water or air cause inclusions, metal contaminations in solid form (dross) or liquid form (slag). Usually metal oxides, nitrides, carbides, calcides, or sulphides come from material originating from furnace (or crucible), ladle linings or mould [24].

2.6.5 Recommendations for high quality casting, crucible and mould material

Campbell has suggested pertinent rules for casting termed “the 10 rules of casting” to follow for quality casting processes [41]. Advanced machinery and automated process control systems have replaced traditional methods of casting. Modern foundries have automated and computer-integrated facilities for all aspects of their operations. Kalpakjian explained the thixotropic behaviour of alloys, which is the fact that viscosity decreases when the liquid metal is agitated, leading to improved castability as does the stirring effect in induction melting. Furthermore, the lack of convection affects the solidification structure and the distribution of impurities [42].

For a specific application, based on chemical, thermodynamics and material science concerns, the following mould and crucible properties must be checked: melting point, thermal shock resistance, oxidation, contamination, thermal expansion coefficient, porosity, shape and size, moisture, chemical reactivity with the melt, air or atmosphere, corrosion, creep resistance, magnetic properties, electrical properties, and compatibility [14,42]. For high quality applications, metals are subjected to refining processes to reduce segregation and inclusions. Fusion under vacuum treatments such as VIM (vacuum induction melting), VAR (Vacuum Arc Re-melting) are used. ESR (Electro Slag Refining) may be required as well. Stainless steels with

low contents of carbon, nitrogen and hydrogen are processed with electric furnaces followed by heat treatments and AOD or VOD (Argon or Vacuum Oxygen Decarburizing). To address the influence of other alloying elements, William D. Callister showed that the eutectoid temperature strongly depends on alloying elements [29]. Jean Callebaut suggested an induction crucible furnace essentially consisting of a crucible with refractory lining containing the material to be melted and surrounded by an induction coil. William Callister listed some pertinent properties of graphite to show that it is a good candidate for induction heating crucible or casting moulds for metal alloys and ceramics, for high-temperature refractories and for insulations [43]. The desired properties of graphite include high strength, good chemical stability at elevated temperatures and in oxidizing atmospheres, high thermal conductivity, low coefficient of thermal expansion, high resistance to thermal shock, high adsorption of gases, and good machinability.

2.7 Theory of induction heating, induction melting

2.7.1 Basics

Electromagnetic induction and the Joule effect are used to heat and melt electrically conductive materials (metals); the heat is generated in the heated material itself. Electromagnetic induction is based on the Faraday-Lenz law, which states that, in a loop of conductive material placed in an alternating magnetic field, an AC current is induced. In practical applications in many cases, a solenoid or coil powered by a frequency converter is used to generate the magnetic field. Mathematically the Faraday-Lenz law is defined by the following formula:

$$E = -N \frac{d\emptyset}{dt} \tag{2.10}$$

Where E is the voltage (V), Φ the magnetic flux (Wb), t is the time (second), and N is the number of turns of the helical coil. According to the same law, eddy current caused by E flows in the opposite direction to that of the supplied current and this justifies the minus sign. Following this law, Jean Callebaut [44] and S. Zinn [45] placed a massive conductor (cylinder) in the alternating magnetic field as seen in Figure 2.3a. They observed varying levels of eddy current along the cylinder radius and succeeded in heating the conductor to the required temperature.

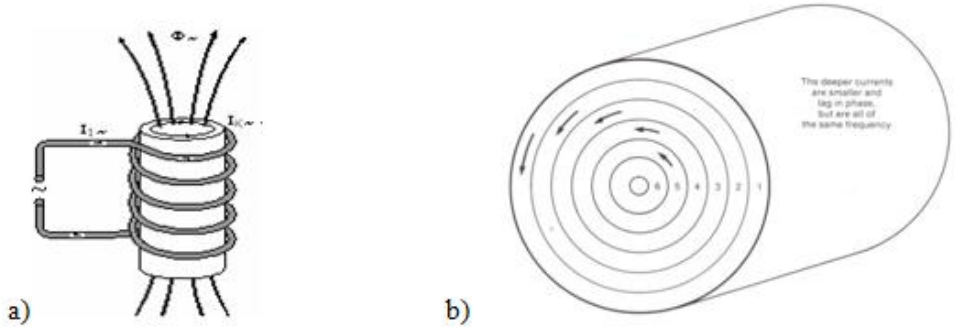

Figure 2.3: a) cylindrical massive conductor in an induction coil [44], b) Eddy-current distribution in a solid cylindrical bar [45]

2.7.2 Advantages and limitations of induction heating [4, 46]

Induction heating offers a number of advantages over convection and radiation furnace techniques. The main advantages include: safe and clean working conditions, low maintenance requirements, very high temperature achievable locally, high quality and purity achievable, under vacuum or inert atmospheres, no production of flue gasses;

Quick heating because of intensive and concentrated local heating, which provides convection and radiation, processes that take place over a much larger volume;

Scale loss since rapid heating significantly reduces exposure time in air during the heating ramp; Fast start-up as convection and radiation furnaces contain large amounts of refractory materials that must be heated during start-up resulting in large thermal inertia. The internal heating of induction process eliminates this problem and allows much quicker start-up.

Energy savings come from the fact that, when not in use the induction power supply can be turned off because restarting is quick. With other furnaces, energy must be supplied continuously to maintain temperature even during production breaks in order to avoid long start-up times. High production rates because heating times are short. Other advantages include increased production and reduced labor costs; ease of automation and control reduced floor-space requirements.

The limitations of Induction furnaces are that it implies big investment and is used for relatively simple shapes.

2.7.3 Joule effect and power for conductor heating

According to the Joule effect, when a direct current I flows through a massive cylindrical conductor piece with length L (m), resistivity ρ (Ω.m), and cross-sectional area of the sleeve A_S (m^2), the resistance R (Ω) is

$$R(\Omega) = \frac{\rho\, L}{A_S} \tag{2.11}$$

The power P dissipated in the conductor is

$$P = R\, I^2 \tag{2.12}$$

However, when an alternating current flows, the skin effect leads to eddy current concentration on the outside of the conductor. Consequently, the eddy current, induced in the piece to be heated are biggest on the outside and diminish exponentially towards the center. The skin effect is characterized by the penetration depth or reference depth and denoted "d". S. Zinn defined the reference depth as the distance from the surface of the material to the depth where the induced field strength and current are reduced to 1/e or 37% of their surface values [46]. As seen in Figure 2.4 below, the power density at this point is $1/e^2$ or 14% of its value at the surface, where "e" is the base of the natural logarithm = 2.718.

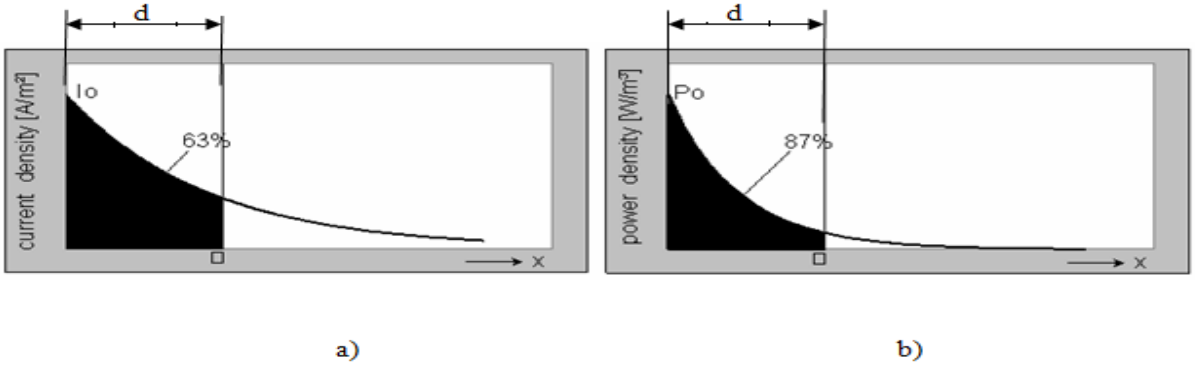

Figure 2.4: Penetration depth as determi as determined using a) current distribution, and b) Power distribution [44]

The definition of the reference depth d is like seen in equation (2.13) [46]

$$d = 5000\sqrt{\frac{\rho}{\mu . f}}\pi r^2 \qquad (2.13)$$

Where d is the reference depth (cm); ρ is the resistivity of the work piece (Ω.cm); μ is the relative magnetic permeability of the workpiece (dimensionless); and f is the frequency of the AC field of the work coil (Hz). For a fixed frequency, the reference depth varies with

temperature because the resistivity of the conductor varies with temperature as well. Furthermore, for magnetic steels, permeability varies with temperature, decreasing to a value of unity at and above the Curie temperature (T_C). Also in magnetic materials, above TC, the reference depth increases with the power density as the steel becomes magnetically saturated and its permeability decreases. Because of these effects, the reference depth in non-magnetic materials (e.g. aluminum) may vary by a factor of two or three over a wide heating range, whereas for magnetic steels, it can vary by as much as 20 factor [46]. Figure 2.5 shows the reference depth for common materials as a function of the frequency for some meaningful temperatures.

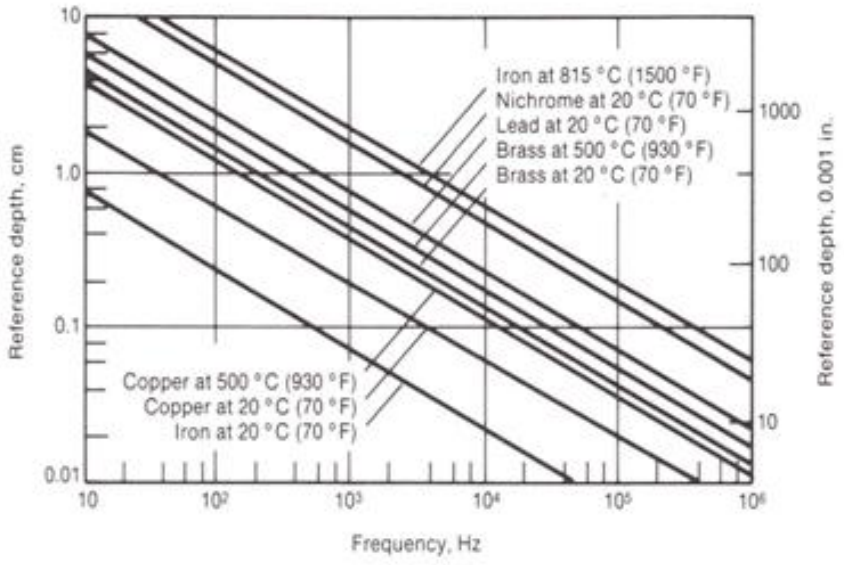

Figure 2.5: Reference depth for common materials as a function of the frequency [46]

2.7.4 Equivalent resistance of solid round bar and electrical efficiency

The equivalent resistance R_{eq} is the workpiece resistance, which, if placed in a series circuit with the induction coil would dissipate as much heat as all the eddy current in the actual workpiece. In other words, the power dissipated in the workpiece would be equal to

$$P = I_C^2 . R_{eq} \quad (2.14)$$

For a solid round bar, it turns out that the equivalent resistance is equal to the product of N^2 and the resistance of a sleeve with one reference depth thickness located at the surface [46]

$$R_{eq} = \frac{\rho \pi a}{A_S} K_{R_2} N^2 \quad (2.15)$$

Where a is the sample diameter; ρ is the resistivity of the work piece K_{R_2} is the resistance factor to account for the electrical path over the reference depth or between the inner and outer diameter of the sleeve. A_S is the cross-sectional area of the sleeve (=d.w) for one coil's turn; K_{R_2} is found for a round bar in Figure 2.6a and for a hollow bar in Figure 2.6b. For a short bar where the length-to-diameter ratio or the work piece diameter-to-coil inner diameter ratio becomes small, another factor Ks_2 (shortness factor), ranked from 0.4 to 1 must be considered in calculating the equivalent resistance [47]. On the other hand, for a given value of R_c, efficiency can be increased by increasing R_{eq}. As can be seen above, skin depth, equivalent resistance and frequency are dependent on the materials properties. The electrical efficiency η is the ratio of electrical energy dissipated in the work piece to that dissipated in the coil.

$$\eta = \frac{R_{eq} \cdot I_c^2}{R_c I_c^2 + R_{eq} I_c^2} = \frac{R_{eq}}{R_c + R_{eq}} \quad (2.16)$$

From which R_c is derived as:

$$R_C = R_{eq} \frac{1-\eta}{\eta} \quad (2.17)$$

This equation demonstrates that for a given equivalent resistance, the efficiency increases as R_C decreases. Because copper has the lowest resistivity of all common metals, it is the typical choice for the construction of induction coils. The following Figure 2.6a shows the relationships

between the workpiece resistance factor $K_{R2}$and the ratio of its diameter over the reference depth for a solid round bar. Figure 2.6b is a similar relationship for hollow tubes.

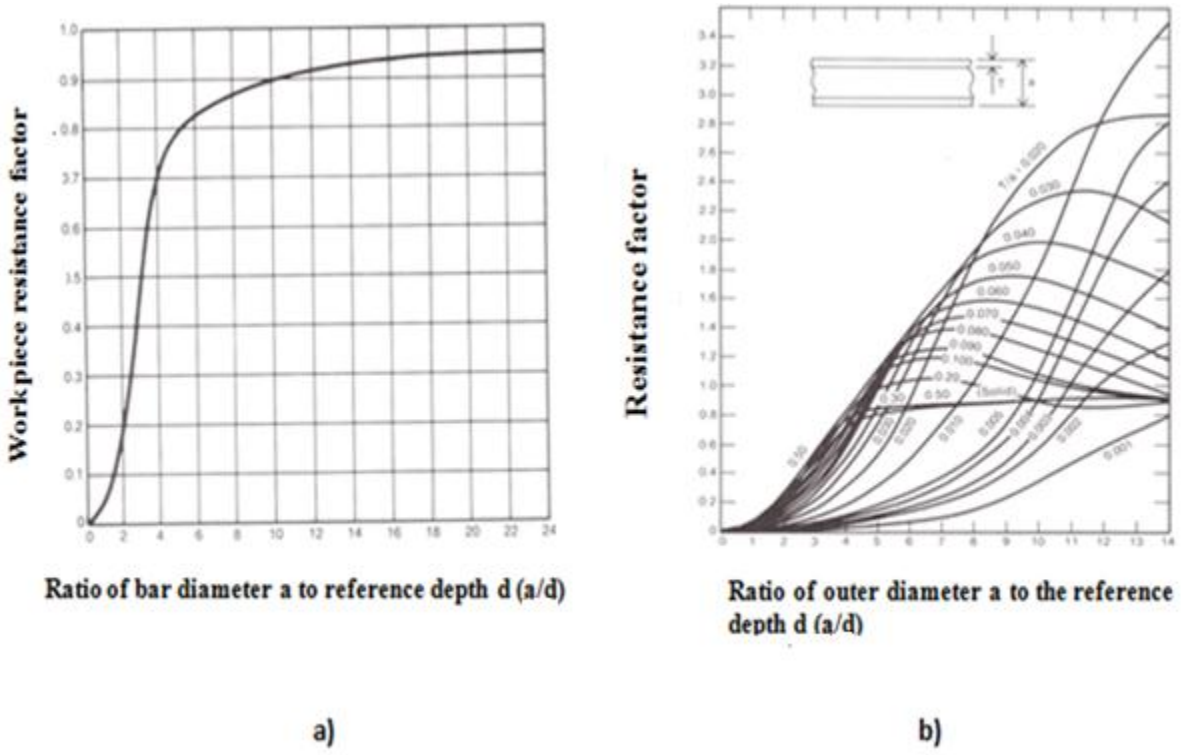

Figure 2.6: Workpiece resistance factor K_{R2} as a function of the ratio a/d for: a) round bar, b) hollow tube for a given ratio T/a [47]

For a/d values below 4/1, the resistance factor $\pi r^2 K_{R_2}$ increases rapidly and above 4/1 relatively little increase in resistance factor can be gained. The formula for the frequency can be derived from the above and its value for d = a/4 is considered the critical frequency. As can be seen in Figure 2.7, at 100% of the critical frequency, the efficiency is unity. Below the critical frequency, the induction-heating efficiency drops rapidly and above it, there is only a little increase. Figure 2.7displays the relationship between the critical frequency and the bar size (diameter for a round bar).

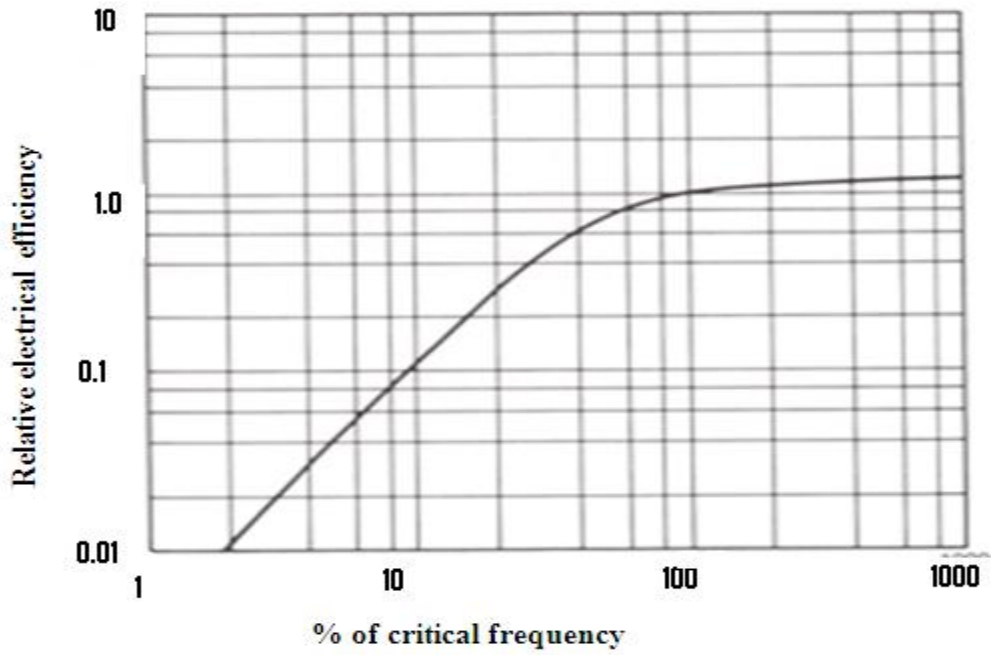

Figure 2.7: Change in heating efficiency as function of frequency in percentage of the critical frequency [47]

It is clear that the material properties strongly affect melting features, reference depth, frequency and obviously power. The following Table 2.3 gives the main properties to consider for induction melting of steel and aluminum.

Table 2.3: Electric, thermal and magnetic properties [48]

	Steel alloy 1020	**Aluminum**	**Graphite**
Thermal expansion (10^{-6} ^{o}C)	11.7	23.6	2.0 to 2.2.7
Thermal conductivity (w/m-K)	51.9	180	130 to 190
Specific heat (J/Kg-K)	486	896	830
Electrical resistivity (10^{-8} Ω-m)	16.0	3.7	10
Magnetic permeability	before Tc (~743^{o}C) 100	1	1
	Above Tc : 1		

2.7.5 Coil design: basic considerations

Some values for Ks_2 considered in the definition of the equivalent resistance R_{eq} are shown in the following Figure 2.8 showing the effect of the air gap and shortness or turns spacing.

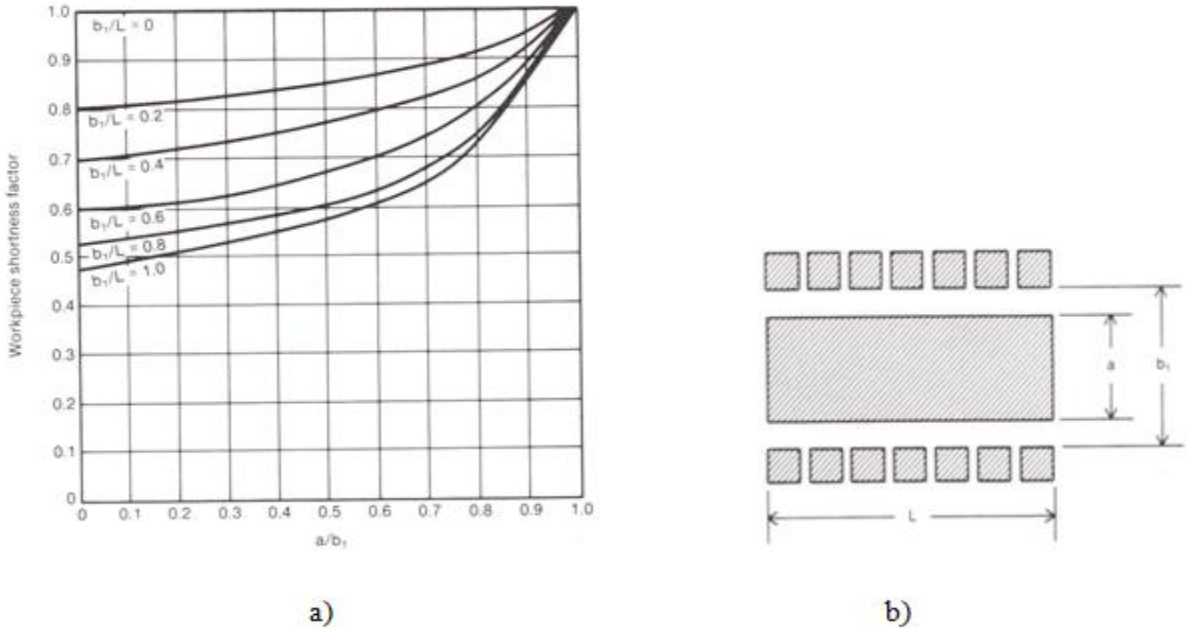

Figure 2.8: a) Workpiece shortness correction factor for solid round and short bar as a function of workpiece diameter-to-coil inner diameter ratio for a given length; b) coupling coil workpiece [47]

Some values for Ks_2 considered in the definition of the equivalent resistance R_{eq} are shown in the above Figure 2.8 showing the effect of the air gap and shortness or turns spacing.

The efficiency of coupling between the windings is inversely proportional to the square of the distance between them. Therefore, the coil should be coupled to the part as closely as feasible for maximum energy transfer. In addition, the denser the flux, the higher the current generated in the part. Therefore, it is desirable that the largest possible number of flux lines intersect the workpiece at the area to be heated. The greatest number of flux lines in a solenoid coil is toward the center of the coil. The flux lines are concentrated inside the coil, providing the maximum

heating rate there. At the point where the leads and coil join, the magnetic field is weaker; therefore, the magnetic center of the inductor is not necessarily the geometric center. Due to this phenomenon and impracticability of always centering the part in the work coil, the part should be offset slightly toward this magnetic area. In addition, the part should be rotated, if practical, to provide uniform exposure.

Table 2.4: Typical coupling efficiencies for induction coils [47]

Type of coil	Coupling efficiency at frequency of			
	10Hz		450kHz	
	Magnetic steel	Other metals	Magnetic steel	Other metals
Helical around workpiece	0.75	0.50	0.80	0.60
pancake	0.35	0.25	0.50	0.30
Hairpin	0.45	0.30	0.60	0.40
One turn around workpiece	0.60	0.40	0.70	0.50
Channel	0.65	0.45	0.70	0.50
Internal	0.40	0.20	0.50	0.25

In general, helical coils used to heat round workpieces have the highest values of coil efficiency and internal coil has the lowest.

2.7.6 Determination of power requirements or power transferred into the workpiece

S. Zinn has established a formula to determine the power required for induction heating [44] as follows.

$$\mathrm{P} = P_1 + P_{rad} + P_{conv} + P_{Coil} \tag{2.18}$$

$$P_1 = W\, c\, \Delta T \tag{2.19}$$

Where, P is the total power needed from the AC power source to the induction coil; W is the total weight to be heated per unit time; c is the specific heat, ΔT is the change in temperature; P_{rad} is the power loss from the work piece due to the radiation. P_{conv} is the power loss from the

work piece due to convection; P_{coil} is loss in the coil due to joule heating. The heat power P_{conv} lost by convection is very small and can be neglected [47].

2.8 Heat treatments

Classified by decreasing cooling capacity, common quenching media include saltwater or brine, water, oil, gases or air. Polymer quenchants can also be used where corrosion and fire risks are to be avoided.

2.8.1 Procedure of heat treatments, microstructure and properties for ferrous metals

Cast parts generally cool relatively fast which does not allow the equilibrium state to be achieved, and the resulting microstructure is often not appropriate for the final application. Therefore, subsequent heat treatments are often needed in order to achieve the desired properties. The purpose of heat treatments is to transform the microstructure of a given material into an optimal state for a given application. With regard to steel, heat treatments generally start with an austenisation followed by cooling to room temperature. Depending on the cooling rate, different microstructures can be formed as summarised in Table 2.5.

Above the critical cooling rate, only martensite is formed. Martensite is strong but brittle with low ductility and toughness. Relatively fast cooling rates just below the critical cooling rate result in a micro-constituent termed bainite (B) which is also fine. Martensite is formed as needles or plates. If a steel alloy having pearlite or bainite microstructure is heated to, and left at a temperature below the eutectoid for sufficiently long period of time (for example 700^{o}C (1300^{o}F) another microstructure called spheroidite forms, where the Fe_3C phase appears as

sphere-like particles. From one phase to the other, the Avrami equation (2.20) is used to assess the time progression of phase transformations.

$$y = 1 - \exp\ (-kt^n) \tag{2.20}$$

Where, k and n are time-independent constants for the particular reaction. Also by convention the rate of a transformation is taken as the reciprocal of time required for the transformation to proceed halfway to completion, $t_{0.5}$:

$$Rate = {}^{1}/_{t_{0.5}} \tag{2.21}$$

Table 2.5: Summary of microstructures and mechanical properties of iron-carbon alloys [48, 49]

Micro constituents	Phases present	Arrangement of phases	Mechanical properties
Spheroidite	α – Ferrite+ Fe_3C	Relatively small Fe_3C sphere-like particles in an α– ferrite	Soft and ductile
Coarse pearlite	α – Ferrite+ Fe_3C	Alternating layers of α – Ferrite and Fe_3C that are relatively thick	Harder and stronger than spheroidite, but not as ductile as spheroidite
Fine pearlite	α – Ferrite+ Fe_3C	Alternating layers of α – Ferrite and Fe_3C that are relatively thin	Harder and stronger than coarse pearlite, but not as ductile as coarse pearlite
Bainite	α – Ferrite+ Fe_3C	Very fine and elongated particles of Fe_3C in an α – Ferrite matrix	Hardness and strength greater than fine pearlite; hardness less than martensite; ductility greater than martensite
Tempered martensite	α – Ferrite+ Fe_3C	Very small Fe_3C sphere-like particles in an α – Ferrite matrix	Strong; not as hard as martensite, but much more ductile than martensite
Martensite	Body-centered tetragonal, single phase	Needle-shaped grains	Very hard and very brittle

The main annealing methods for steels include normalizing, austenitizing, and full annealing as illustrated in Figure 2.9 [48], as well as spheroidizing and decarburizing. The eutectoid

temperature is conventionally labelled A_1 (lower critical temperature) under which all austenite will have transformed into ferrite and cementite phases if equilibrium conditions are met.

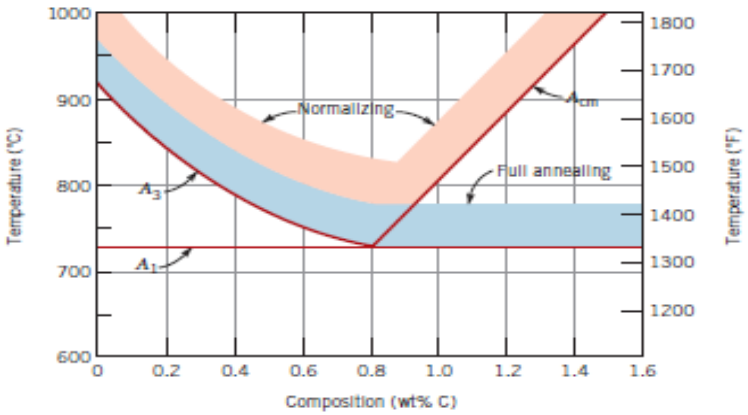

Figure 2.9: Heat-treating temperature ranges for plain carbon steels [48]

The phase boundaries A_3 and A_{cm} represent the upper critical temperature lines, for hypo-eutectoid and hypereutectoid steels, respectively. Above these boundaries, only the austenite phase prevails. Additionally, other alloying elements can shift the eutectoid and the positions of these phase boundary lines. To improve steel workability, normalizing is accomplished by annealing to at least 55^{o}C above the upper critical temperature that is above A_3 for hypo-eutectoid composition and above A_{cm} for compositions greater than eutectoid. After sufficient time is allowed for the alloy to completely transform to austenite (austenitizing), the treatment is terminated by cooling in air. For forming operation purposes, full annealing is used to improve machinability and malleability of carbon steels. The alloy is heated to a temperature of about 50^{o}C above the A_3 line to form austenite for compositions less than eutectoid, or, for compositions in excess of the eutectoid, 50^{o}C above the A_{cm} line to form austenite and Fe_3C. The alloy is then furnace cooled for several hours to allow the whole austenite to transform to coarse pearlite that is relatively soft and ductile. The full-anneal cooling procedure is time consuming; however, a microstructure having a uniform grain structure is the result.

During spheroidizing there is a coalescence of Fe_3C to form the spheroide particles; it can be performed by annealing the alloy at a temperature just below the eutectoid in the alpha + Fe_3C region. If the precursor microstructure contains pearlite, spheroidizing time will ordinarily range between 15 and 25h. Another method is heating to a temperature just above the eutectoid temperature, and then either cooling very slowly in the furnace, or holding for a given duration. A final method is alternately heating and cooling within about + or – 50^{o}C of the A1 line [48].

Maraging (martensite age hardening) is a process that consists to precipitate one or more inter-metallics in a matrix of low carbon martensite. It does not depend on cooling rate and causes minimal distortion. For this reason maraged structures are used for die, and tooling for casting, forming, moulding, forging and extrusion [49]. Decarburization is a phenomenon in which alloys lose carbon from their surface because of heat treatment or of hot working in a medium (usually oxygen) that reacts with carbon. Since this reduces the hardenability, hardness, strength and fatigue life, it is best avoided by processing the part in an inert atmosphere, in vacuum, or by using neutral salts during heat treatment [49].

2.8.2 Heat treatment procedure for aluminum and other nonferrous alloys and stainless steels

Non-ferrous alloys do not undergo phase transformations like steels and cannot be heat treated by the techniques used for ferrous alloys [49]. Heat treatable aluminum alloys, copper alloys, martensitic stainless steel, and some other stainless steels are hardened by precipitation hardening. In this process, the solid solubility of one element (solute) of the alloy in the other (solvent) is exceeded; and consequently small particles of a different phase called precipitates are created and dispersed uniformly in the matrix of the original phase. Precipitation hardening of an alloy of 95.5 wt% Al and 4.5wt%Cu is described in Figure 2.10. Between 500 and 570^{o}C, there exist single-phase substitution solid solution which is ductile and has FCC structure. Below the

lower solubility curve, there are two phases: kappa phase (k) and a hard inter-metallic compound of CuAl2 (θ). During heat treatment, the properties of the alloy are modified by solution treatment and precipitation. Nonferrous alloys' heat treatments encompass precipitation hardening which in turn consist of solution treatment and age hardening as shown in Figure 2.10. The alloy is heated and kept within the solid solution kappa (k) phase, for example 540^{o}C, and then cooled rapidly by quenching it in water. The structure obtained shortly after quenching consists of only the single-phase kappa. This alloy has moderate strength and considerable ductility. During age or precipitation hardening as subsequent process**,** the alloy is reheated to an intermediate temperature in the two phase region and held there for a period, during which precipitation takes place. The solute atoms diffuse to the nucleation sites and combine the solvent atoms to form the theta phase as sub-microscopic precipitate B seen as small dots in grains.

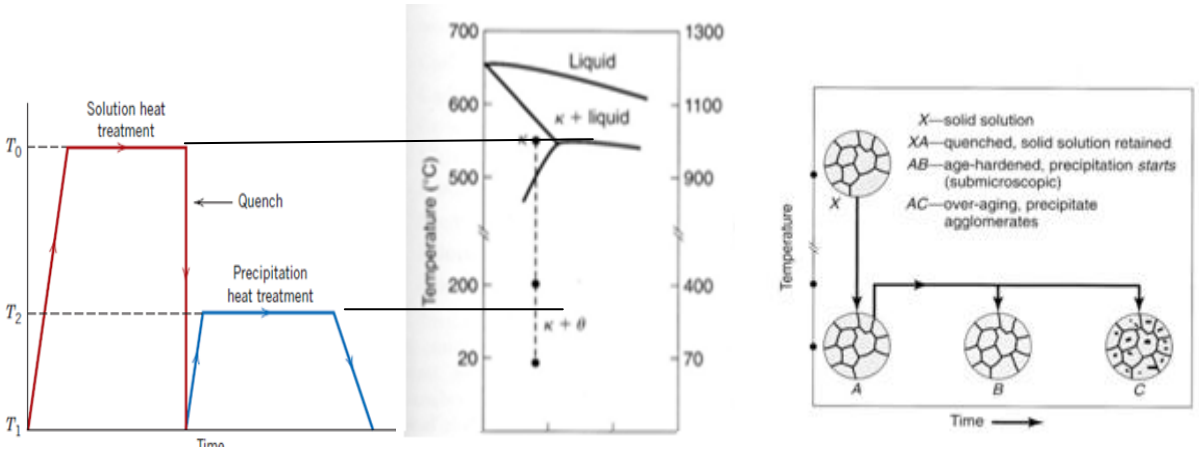

b)

Figure 2.10: a) Time-temperature graphs for heat treatments and relevant phase diagram [48]; b) various microstructures obtained during the age-hardening process [49].

With increasing aging time, strength and hardness first increase, reach a plateau, and then fall when over-aging starts. This shows that there is an optimal time in the ageing process that must be achieved in order to obtain desired properties [50].

2.9 Wear resistance, hardness, toughness, tensile strength and ductility

2.9.1 Correlation between wear resistance, hardness, toughness and ductility

Wear phenomena are very complex and depend on both material properties and environment. It is primarily mechanical in nature but chemical reactions may also be involved. Mechanical wear may be defined as a surface deterioration and/or material loss caused by stresses arising from contact between the surfaces of two bodies. Correlation of harness and wear comes from the fact that, during relative sliding contact of two bodies (one harder than the other), wear is closed by the removal of material from the softer body due to contact with the harder one.

On the other hand, if the friction time is too long, increase in temperature also occurs and contributes to change the coefficient of friction, the mechanical resistance and the microstructure of the material, which affect the wear resistance. There is also a relation between wear and fatigue [7, 19]. In this case, mass loss may result from cyclic stresses caused by the relative motion of two contacting bodies. This can cause the disruption of very small areas that bond and break as the surfaces undergo friction, often in the presence of vibrations. The bonding contact areas deform under the localised pressure and the two surfaces gradually wear away. It may start with flaws nucleation, and once these flaws exceed the critical condition, fracture propagates across the whole structure. The correlation between wear and tensile modulus and toughness is

given by fracture mechanics. According to this concept, each localised fracture has to satisfy the general rule, which states that, the elastic energy released as the bond fractures must exceed the work done in plastically deforming it and in creating the fracture surfaces.

Fracture toughness is a property that describes the ability of a material containing a crack to resist fracture. So if a material has high fracture toughness it will probably undergo ductile fracture. Brittle fracture is very characteristic of materials with less fracture toughness [7, 19]. A related concept is the work of fracture (γ_{wof}) which is directly proportional to

$$\frac{K\, I_C^2}{E} \tag{2.22}$$

Where E is the Young's modulus of the material in SI units, γ_{wof} is given in J/m^2. The value of fracture toughness K_{Ic} for aluminum ranges from 14 to 28 MPa-m$^{1/2}$ while, for steel it is around 50 MPa-m$^{1/2}$.

2.9.2 Hardness testing and correlation between hardness number and tensile strength

To determine the localized deformation of a material, hardness test is performed over its surface. Test conditions include a given duration, a known load that is applied on an indenter (made of a chosen material harder than the one to test) with a specific size and geometry. After the test, there is a small indentation on the surface being tested. The depth and size of the indentation is related to a number; the softer the material, the larger and deeper the indentation and the lower the hardness number. As the conditions change with various applications, four main different techniques are used for hardness testing. Brinell (conical indenter), Vickers and Knoop (small diamond, pyramidal indenter), and Rockwell (spherical indenter of different sizes and loads as well as different load scales). Hardness testing is simple, inexpensive, and non-

destructive as out of the small indentation (resolution for Vickers hardness is in the order of nm or μm), the specimen is neither fractured nor excessively deformed. For these reasons, hardness tests are frequently used for primary investigations that provide hardness data, from which other mechanical properties may be estimated. For metallic materials, ASTM standard E140 provides testing conditions and conversion tables between hardness numbers of the different techniques. Vickers hardness testing, compared to other techniques, produces a pyramidal dent, more accurate measurement that in turn gives a more precise hardness number. Both tensile strength and hardness are indicators of materials resistance to plastic deformation. They are therefore proportional [51]. For steel alloys, conversion of Brinell hardness HB to tensile strength TS, is estimated according to the relation equation (2.23):

$$TS(MPa) = 3.45HB \tag{2.23}$$

For hardness numbers in the range of 100 to 1000, Vickers (Knoop) hardness are almost identical to Brinell hardness [51], so equation (2.23) can apply to Hv as:

$$TS(MPa) = 3.45Hv \tag{2.24}$$

2.10 Conclusion

From the above literature review, a general observation is that extensive work has been done on Al-Fe inter-metallics. For some specific applications, killed-steel involving addition of some aluminum in steel to inhibit carbon effects has been used, but practically no research has focused on solid solution Al-Fe alloys to date. In addition, most research has focussed on iron rich inter-metallics while very little has been done on the aluminum rich–side of the system. In

addition, intensive research efforts are still being made to optimize the room-temperature ductility and strength of aluminum-steel alloys.

3 EXPERIMENT

3.1 Initial materials

Table.3.1 summarises the properties of the two initial materials used in this study: aluminum 6061T6 and steel 1020. The two materials were primarily selected because of their relatively low alloying element contents, which make them ideal for investigating the potential of manufacturing recycled Al-Fe based alloys. The materials were taken from waste stocks from the University machine shop in 8 mm rods for 6061T6 aluminum and 6 mm rods for 1020 steel.

Table 3.1: Density, strength elongation, elastic modulus, and Poisson ratio of aluminum alloy 6061T6 and steel 1020 [48, 53]

Designation (units)	Steel (1020)	Aluminum (6061 T6)
Treatment	Normalized 925^{o}C	Heat treated (HT) and aged
Density (g/cm^{3})	7.80	2.71
Yield Strength (MPa)	345	276
Strength (MPa)	440	310
Percent elongation	38.5	17
Elastic Modulus (GPa)	207	69
Melting temperature (^{o}C)	1563	667
Curie temperature (^{o}C)	746	Not applicable
Composition	0.2C,0.45Mn,	1.0Mg, 0.6Si, 0.30Cu, 0.20Cr, 0.5Fe [53]

Samples were cast with compositions selected using the Fe-Al phase diagram (Figure 2.2). As seen in this diagram, inter-metallics prevail in large ranges of compositions, primarily from 12wt% Al to ~100 wt% Al. Although showing good properties and potentials for intermediate and high temperature applications, inter-metallics are known to be brittle for many low temperature applications. As the current study focuses on recycling Fe and Al alloys for standard use primarily at room temperature, no or only minimum fractions of intermetallic precipitates are desired. Therefore, the two types of alloy compositions selected are, one steel-rich alloy (TN4)

made by addition of 10wt%6061T6 into steel 1020, and aluminum-rich alloys (TN3 and TN5) made by addition of either 0.7wt% or 5wt% steel 1020 into aluminum 6061T6. The different alloy mixtures and material codes are provided in the following Table 3.2.

Table 3.2: Compositions of the alloys investigated [52]

	Steel-rich	**Aluminum-rich**	
Composition/ casting	90wt%1020+ 10wt%6061T6	95wt%6061T6+ 5wt%1020	99.3wt%6061T6+ 0.7wt%1020
Code	TN4	TN3	TN5

3.2 Casting equipment

Casting was done using an induction heating system, a Tucker induction power supply system, model 3-135/400-3W (Figure 3.1). It provides a maximum power of 3KW and a frequency range between 135 and 400 kHz. A frequency of 400 kHz is used for low energy operations while frequencies down to 135 KHz are appropriate for high energy heating and melting (most thicker workpieces). Table 3.2 shows some specifications of the power supply unit.

Figure 3.1: Induction heating system model 3-135/400-3kW [52]

Table 3.3: Input and output of induction supply system [52]

Input		Output	
AC line to line voltage	208V-240V	Maximum voltage	350V
AC line current	14.5A at 230 V	Duty cycle	100%
AC Power	3.6 kVA	Maximum power	3kW
Frequency	50 to 60 Hz	Frequency	135 to 400 kHz

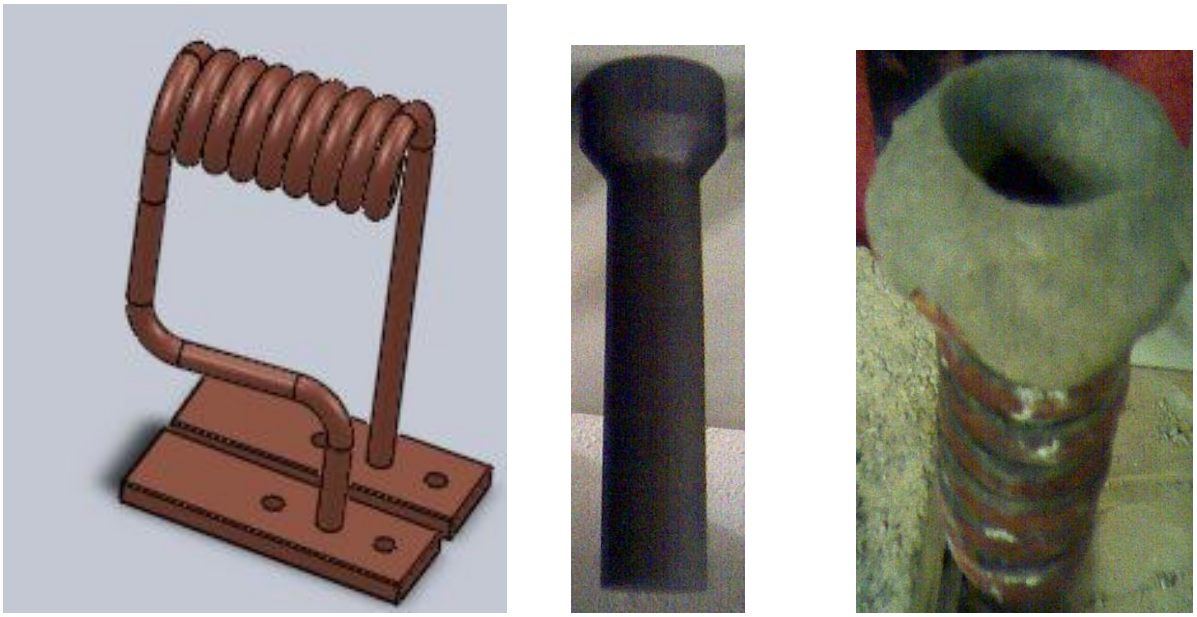

a) b) c)

Figure 3.2: a) Induction heating coil; b) Graphite crucible; c) Lining and insulating clay-seat formed on the heating coil

A copper heating coil with an inner diameter ID of 26.5 mm, a mean diameter MD of 30 mm, and 8 turns over an 80 mm length was used. It was manufactured using a copper tube with 6 mm diameter channel for water-cooling and 8 mm outer diameter. The copper tube was wrapped around a 1-inch steel pipe to create the initial spiral form. The spiral was annealed for softening using oxyacetylene torch and was then freely wrapped and squeezed by hand to the desired coil

diameter (that provides smallest air gap between the coil and the crucible), turn spacing (turns as close as possible), and length. The heating coil was attached to the AC power supply system using a custom-built copper mounting plate.

To measure or control the temperature, a Whatlow 96 thermocouple with a maximum temperature capacity of 1300^{o}C (2372^{o}F) was used. It served for temperature measurements up to 1200^{o}C and to calibrate the Leed &North Rup Co Optical pyrometer that was used for higher temperature measurements.

Figure 3.3: Set-up showing the argon supply for corrosion protection during casting: a) argon tank; b) argon pipe and stand; c) argon flow and pressure regulator.

Graphite was selected as crucible material due to its excellent thermo-shock resistance. In contrast to oxide crucibles that tend to crack during rapid heating, graphite crucibles can survive multiple rapid heating and cooling cycles. A further advantage of graphite is its excellent thermal and electrical conductivity, which enables efficient heating of non-magnetic materials that necessitate external heating due to the difficulty to generate sufficient eddy current in them since there is no hysteresis to generate extra heat as in ferromagnets. This is the case for non metallic

materials, steel above the Curie temperature and aluminum in general. Crucibles (Figure 3.2b) were made by machining a 1-inch diameter graphite rod to the desired inner (12 mm) and outer (16 mm) diameters. The selected combination of induction coil and crucible dimensions were found to ensure sufficient magnetic field density for induction heating while providing sufficient crucible wall thickness for mechanical stability and appropriate crucible volume for the desired sample dimensions. Different challenges had to be met in order to ensure proper induction heating of the samples: First, the power limitation of the induction power supply at 3 kW that did not allow fabrication of large samples. This was addressed by using relatively short induction coils with a small turn diameters. This meant the cast sample diameters had to be reduced and the crucible had to be moved axially during casting in order to fabricate longer samples in a quasi-zone-by-zone or section-by-section melting process along the sample length. Second, due to the high electrical conductivity of graphite, contact between the crucibles and the induction coil had to be avoided in order to prevent short-circuiting. Therefore, a clearance of 2 mm had to be provided which was practically filled by an amorphous clay lining applied around the inner perimeter of the induction coil and served as insulation (Figure 3.2c). Third, although a constant flow of gas was used to purge the crucibles and prevent oxidation and corrosion during casting, the external surface of the crucibles was not completely protected and suffered substantial oxidation and mass loss at high temperatures. This was addressed by providing sufficient wall thickness of the crucibles that ensured that the crucibles do not fail or be perforated by corrosion during casting. The wall thickness was designed for only one single cast survival since it had to be destroyed anyways in order to remove the cast samples.

Depending on the material load (material type and quantity) to be molten, the power supply was tuned by adjusting the inductance in order to achieve the maximum power of 3 kW at a current density of maximum 50 A as suggested by the manufacturer. This allowed the system

to operate optimally and prevent overheating. Coarse and fine-tuning of the inductance are done

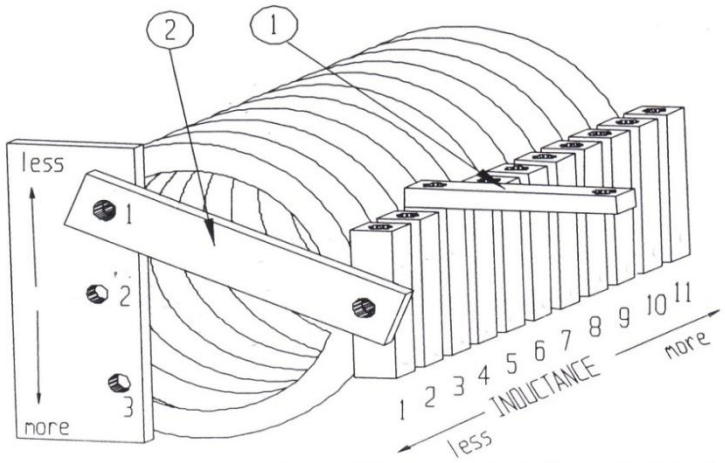

Turn selector bar (0 -11 turns) Variable shorting bar

by positioning levers 1 and 2 respectively as illustrated in Figure 3.4.

Figure 3.4: Inductor in the Tucker induction power supply system and its tuning bars [52].

3.3 Casting and heat treatment process

For casting, the crucible was first purged with argon for 2 minutes. Material pieces of 1020 steel and 6061T6 aluminum were then loaded into the crucible piece by piece in order to allow a continuous evacuation of air during loading. The power was then applied for melting and the casts were left to cool in the crucible that, by so doing served as mould.

Heat treatments were performed using a Lindberg/Blue electric furnace with a temperature range of up to 1200^{o}C. To normalize the steel-rich casts TN4 (10 wt% 6061 + 90wt%1020), samples were heated to 980^{o}C, maintained for 4 hours, and then cooled either in air or in standing water; the related chart {a b c d} is shown in Figure 3.5A. For precipitation hardening

of aluminum-rich samples, TN5 (0.7 wt% 1020 + 99.3wt% 6061) was heat treated following chart {1234} at 600^{o}C for 4 hours and underwent ageing following chart {4567} at 232^{o}C for 1 hour as shown in Figure 3.5 B.

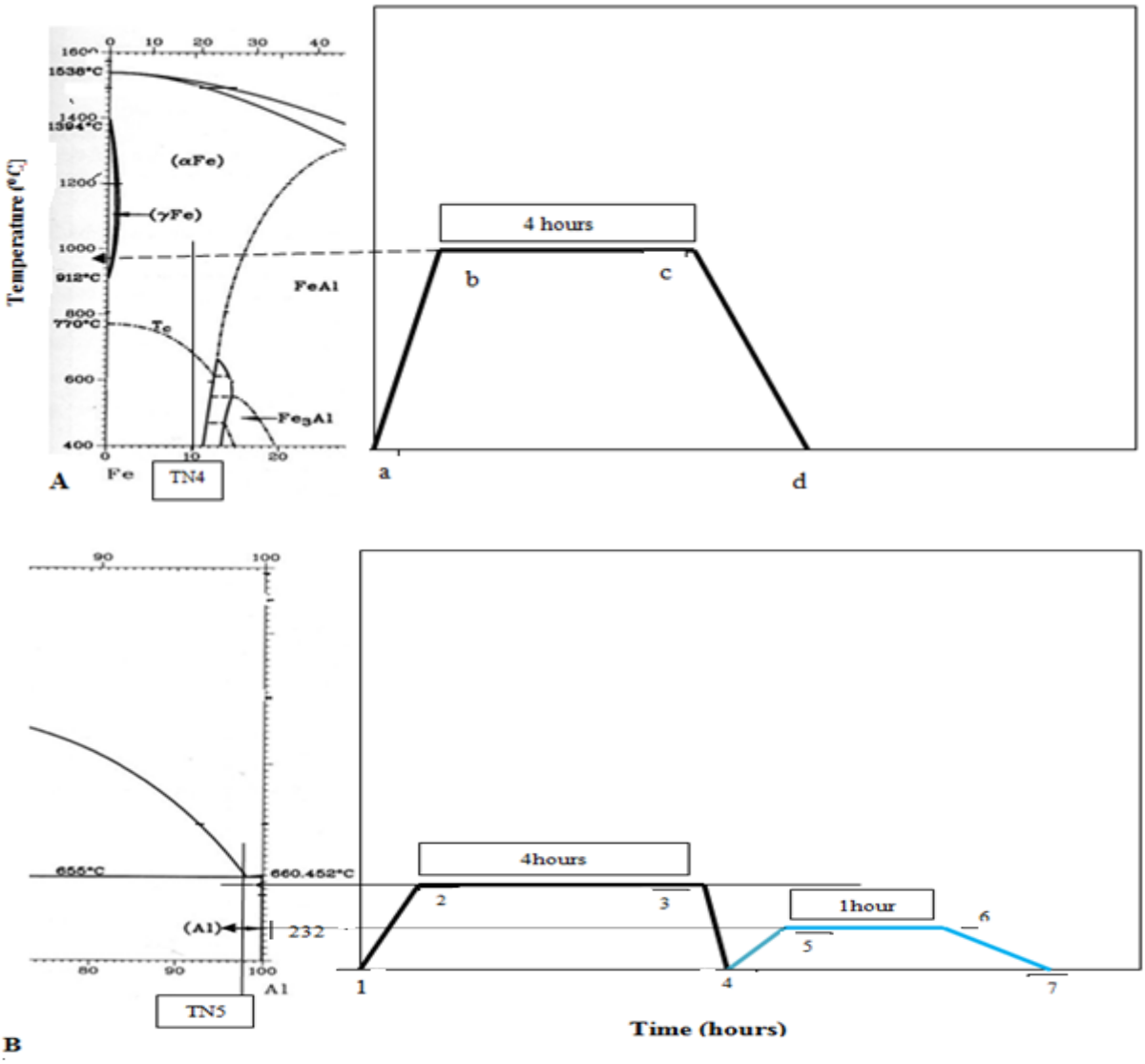

Figure 3.5: Sequences for the heat-treatment of: A) Steel-rich and B) Aluminum rich cast alloys.

One set of aluminum samples was only solution heat-treated at 600^{o}C for 4 hours and then either water- or air-cooled. A second set of aluminum samples was solution heat treated and air

cooled similar to the first set and was then given an additional ageing heat treatment at 232^{o}C for 1 hour, and then air cooled.

3.4 Metallographic sample preparation and microscopy

Metallographic sample preparation involved cutting samples from the initial rods or from the cast samples, mounting, grinding and polishing. Cutting was carried out using a digital controlled STRUERS Secotom-10 with a spindle speed of 2000 rpm and either diamond or silicon carbide cutting plates. The samples were mounted in epoxy resin using a STRUERS LaboPress-3.set machine. A STRUERS Tegrapol-31 machine was used for grinding and polishing. The polishing parameters were 2000-rpm disc speed, single sample, manual preparation, group 2. Grinding and polishing steps (1 to 5) are provided in the following Table 3.4 for aluminum rich and steel-rich samples.

Table 3.4: Grinding and polishing program

	Aluminum rich sample	**Steel rich samples**
1	Grinding Piano 120 for 1 minute	Grinding Piano 120 for 1 minute
2	Allegro 9 micrometres, Diamond, for 3 minutes	Largo, 9 micrometres, Diamond, 25
3	Dac (blue color), 3 micrometre, diamond for 3 minutes	Dac, 3 micrometres, 20 N for 3 minutes
4	Nap, 1 micrometre, Diamond	Chen OPS 0.04 micrometres, 15 N
5	Chem, 0.04 micrometre OPS SiC	NA

Appropriate cleaning was done between each two steps using water flushing and an ultrasonic ethanol bath in order to prevent particles from a previous step to cause scratches on the sample. Optical microscopy samples were etched using a Keller's solution for aluminum rich samples and a 2% Nital solution for iron rich samples. The samples were exposed in the etch solutions for 2 minutes or more and then thoroughly cleaned with water, and ethanol, and then

dried. Optical microscopy was performed on an XJP-3A microscope equipped with a Clemex video camera enabling the images to be transferred to a computer. Microscopy images were then imported to the Clemex Vision PE software for analysis. Scanning electron microscopy investigations were performed using a ZEISS electron microscope equipped with an Energy dispersive X-ray spectroscopy (EDX) detector for chemical analysis (SEM EVO-MA10, Zeiss, Germany). The SEM instrument is equipped with electron dispersion spectroscopy detector (INCA-x-act, Oxford Instruments, Abingdon-Oxfordshire, UK) for chemical analysis. Optical and scanning electron microscopy investigations allowed studying sample microstructures including composition, phase and defect identification and analysis. Microscopy studies were performed on initial materials 1020 steel and aluminum 6061T6 as well as on mix alloys fabricated in this project. SEM EDS spot analyses were done at grain boundaries (GB), in grain interiors (B), on precipitates and in porous and defect regions. Hardness indentation regions were also investigated in order to check for potential crack initiations, which could be an indication for material toughness or brittleness.

3.5 Micro hardness, Wear testing, weight reduction

Micro-hardness tests were performed on initial and cast samples at all investigated heat treatment states using a STRUERS DURAMIN A/S DK-2750 micro-hardness-testing machine equipped with an optical objective for direct measurement of indentation diagonals and hardness calculation. An indentation load of 300 g (Hv0.3) and a holding time of 10 to 15 seconds were used. Hardness values were taken from grain interiors, grain boundaries, precipitation and other defect areas as well, along the sample radii in order to assess the deformation resistance and the homogeneity/heterogeneity of the casts. Only the values of interior grain hardness, measured at

five locations of each sample were considered. Their average and standard deviation were computed and plotted as hardness results for the relevant sample as seen in chapter 4.

Figure 3.6 shows the STRUERS DP-U machine used for pin-on-disc wear testing. A disc rotation speed of 1500 rpm and a pressure load of 100 g were used for aluminum and for steel rich samples. A 120 grit SiC grinding paper was used as disc contact surface with the samples being the pin. The grinding paper wears out during testing and heating due to friction might alter the friction coefficient. Therefore, the wear tests were interrupted every 3 minutes and the sample was moved to new positions along the disc radius in order to provide fresh grinding paper surface for a continuous and uniform abrasion. In addition, in order to provide for constant wear intensity, the linear sliding speed (V) was kept constant at 43.96 m/min by adjusting the disc rotation speed (N) for each radial position (r) of the samples. The disc rotation speed (N) was computed according to Equation (3.1) below.

$$N\ (rpm) = \frac{V}{2\pi r} = \frac{43.96\ (^{m}/_{min})}{2\ \pi\ r\ (m)} \tag{3.1}$$

Wear test samples for 6061T6, 1020 and for the new alloys were cylindrical with 8 mm diameter and 16 mm length; they were produced by cutting to length 8 mm diameter rods of initial materials, and by machining cast samples down from their initial 12 mm diameter to the desired 8mm diameter. Machining of the new cast samples also helped remove the oxidised and chemically altered surface.

a) b)

Figure 3.6: a) STRUERS DP-U Wear testing machine, b) Current and speed analog display

Figure 3.7 shows the wear test sample and the sample holder. The holder (Figure 3.7b) fits in the wear testing machine as seen in the Figure 3.6 above. The sample (Figure 3.7a) is centered in the holder (Figure 3.7b).

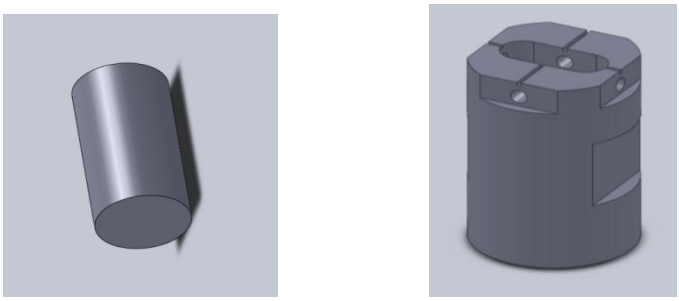

a) **b)**

Figure 3.7: a) Wear test sample, b) Wear test sample holder

A 100-gram load was used for all materials to press the samples on the abrasive disc surface. Thesliding wear distance L is calculated according to Equation (3.2).

$$L = V.t \tag{3.2}$$

where t is the effective wear test duration. The wear resistance was assessed in terms of mass loss per unit time (minute), which is the wear rate. This means, the sample with the higher wear

rate has the lower wear resistance. To measure the mass loss, the tests were interrupted in three-minute intervals; the samples were removed from the sample holder and cleaned in an ethanol ultrasonic bath. The samples height and weight were then measured using a Mitutoyo high-resolution digital calliper and a digital weight-scale respectively.

To assess weight reduction, the percentage of the mass difference of wear samples of the fabricated alloy and that of steel alloy 1020 versus the mass of wear samples of the initial material steel 1020 (M_{1020}) was then calculated as:

$$\%\, mass\ reduction = \frac{\overline{M_{1020}} - \overline{M_{alloy}}}{\overline{M_{1020}}} .100 \qquad (3.3)$$

$\overline{M_{1020}}$, $\overline{M_{alloy}}$ mass mean values were calculated using five samples of 1020 as reference material and five samples of TN4 alloy solutionised and air-cooled respectively.

4 RESULTS

4.1 Microstructure and chemical compositions of aluminum rich samples TN3 and TN5

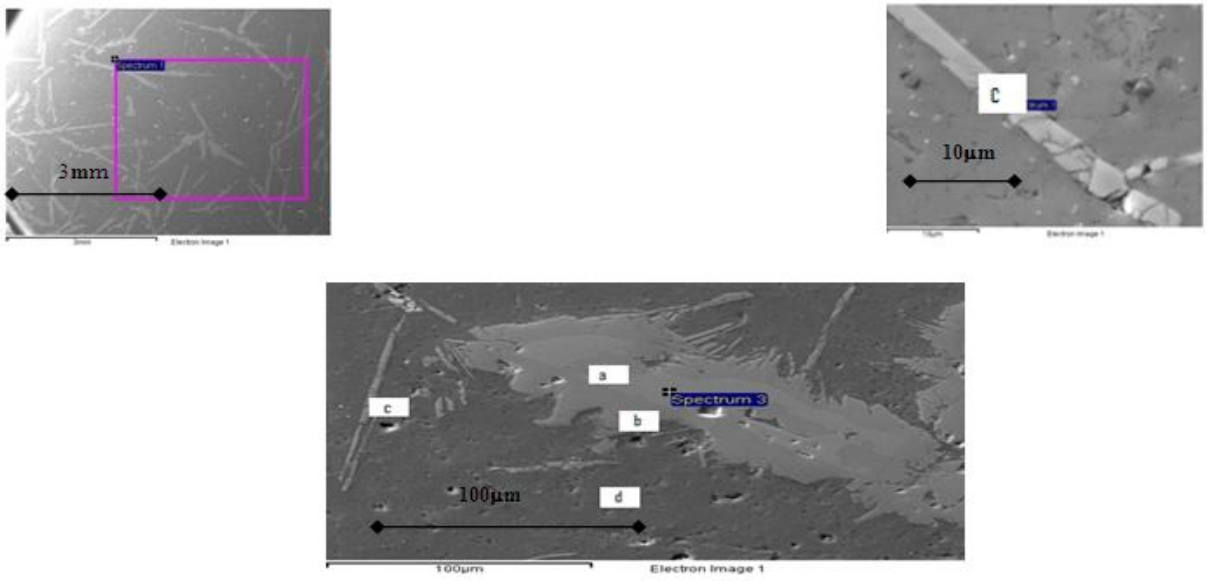

Figure 4.1: Electron image of the cast TN3 with 5wt% 1020 + 95wt% 6061

Table 4.1: Chemical compositions at locations marked on samples TN3, Figure 4.1

	Content in wt% of						
Element	**Al6061T6**	**Steel 1020**	**locations marked (Phase)**				
			a	**b**	**c**	**d**	**Area mapping**
C	0	0.06-1.03	0	0	0	0	3.81
O	0.05-0.5	0	0	0	0	0	1.61
Al	91.8-99	0	59.46	61.47	61.75	96.77	80.70
Si	0.2-1.8	0.15-0.35	2.78	8.68	15.43	1.46	9.63
Ti	0.01-0.25	0	0	0	0	0.26	0
Fe	0.04-1	97-100	37.77	29.31	22.82	0.26	4.26
Ag	0	0	0	0	0	1.25	0
Mn	0.01-1.1	0.25-2.05	0	0.54	0	0	0
Total	100	100	100	100	100	100	100
Ref/Source	[53]	[53]	EDS	EDS	EDS	EDS	EDS

It can be seen on the micrographs in Figure 4.1 and from the chemical analysis results in Table 4.1 that the mixture is deficient in some TN3 samples. There is a high concentration of iron

above 22-wt% at the brighter locations a, b, c, while the darker matrix location d practically contains only elements of the aluminum alloy 6061T6. Between these four locations, the aluminum content varies by 36-wt% while the iron content varies from 0.26wt % to 37.77wt%. Overall, the detected carbon content is higher than in steel 1020. The heterogeneity of the mixture in TN3 is confirmed by the microstructure in Figure 4.2 b where there are large flakes in both the as cast and the heat-treated.

4.1.1 Microstructure in various states of TN3

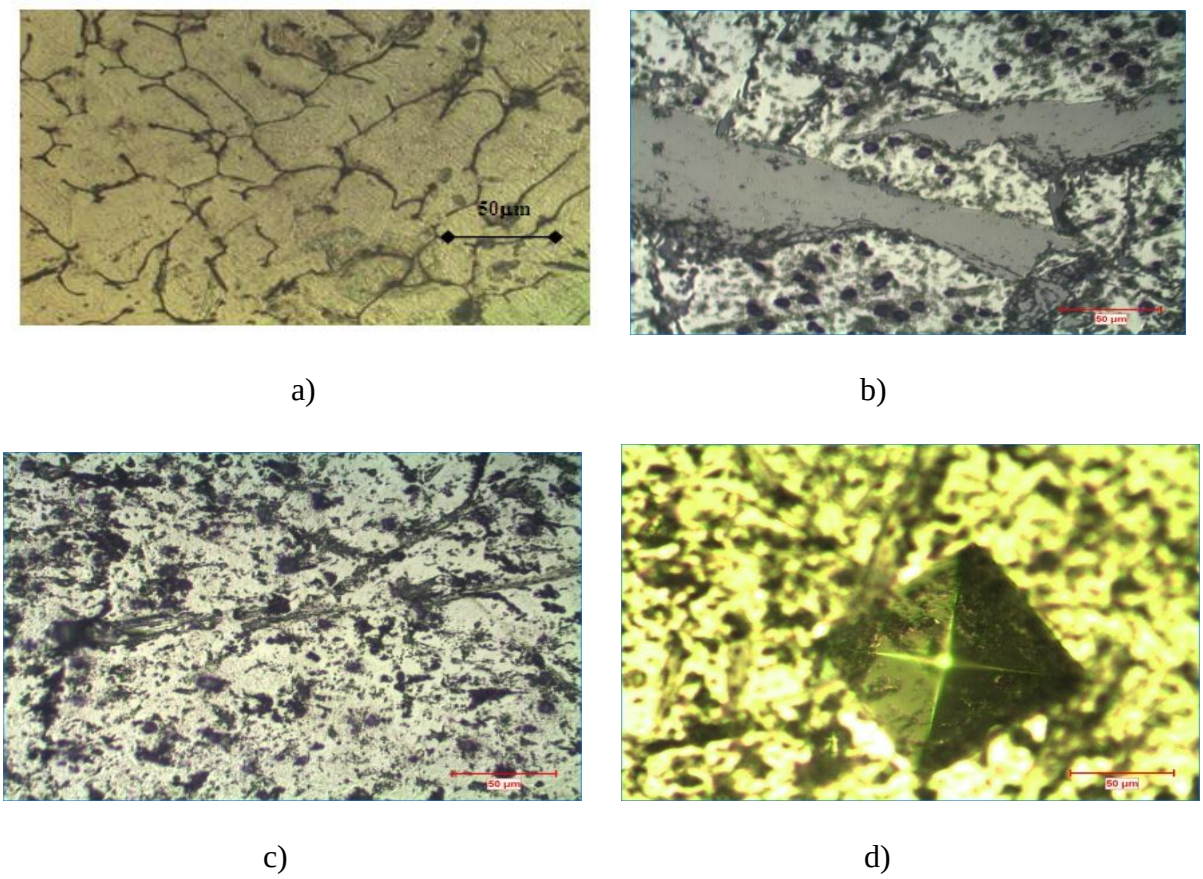

Figure 4.2: TN3 (5wt%1020 + 95wt%6061) in different states: a) as cast; b) and c) aged and water-cooled; d) aged and air-cooled.

4.1.2 Microstructure of various states of samples TN5

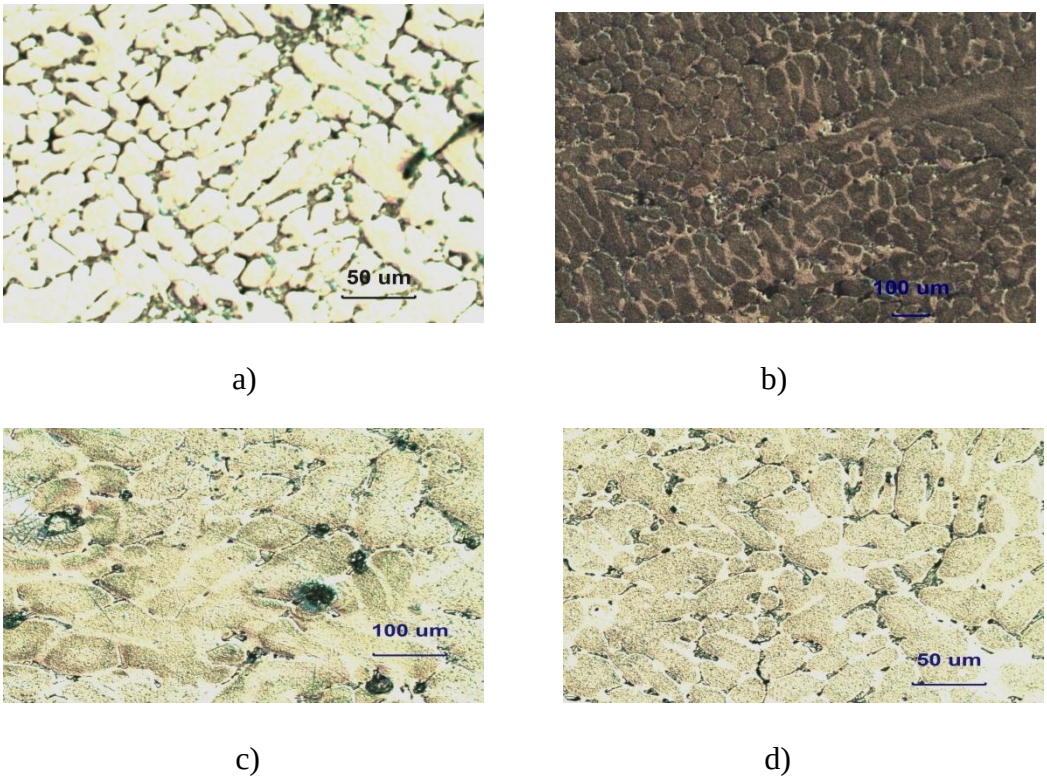

Figure 4.3: TN5 (0.7wt% 1020 + 99.3wt% 6061T6) in different states: a) as cast; b) solution heat treated and air-cooled; c) solution heat treated and water-cooled; d) solution heat treated, quenched, aged and air-cooled.

As-cast TN5 shows fine dendritic cells and small dark and gray silicon particles in interdendritic aluminum-silicon eutectics. After air-cooling grains seem finer while water-cooling and ageing (Figures c and d) form coarser dendrites. Grain boundaries are visible where inclusions are located. Small precipitates (small dots-like) are within the grains of sample TN5 which underwent ageing also called precipitation hardening.

4.2 Microstructure and chemical composition of TN4 (10wt% 6061T6 + 90wt% 1020)

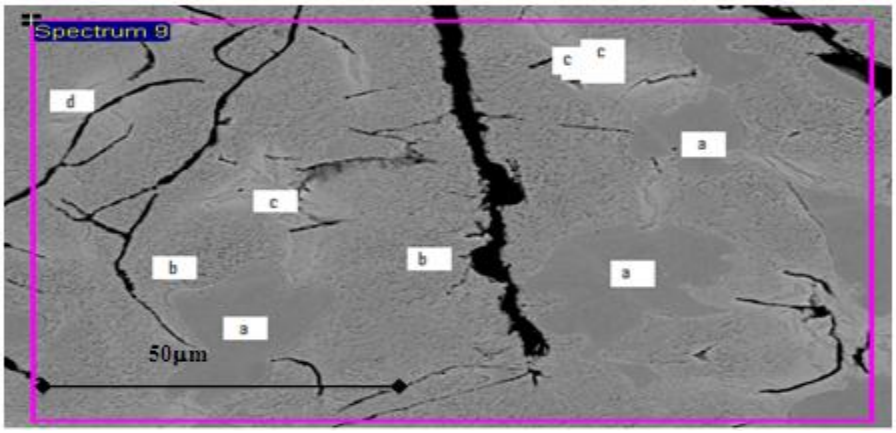

Figure 4.4: Electron microscopy image showing general overview of TN4, different contrasts in sample TN4

Table 4.2: Chemical composition at locations a, b, c and d in figure 4.4 for TN4

	Content of Alloying elements in						
	wt% in base materials		Wt% at location or area of the new alloy TN4				
Element	**Aluminum 6061T6**	**Steel 1020**	**Location a**	**Location b**	**Location c**	**Location d**	**Area**
C	0	0.06 -1.03	6.48	6.62	2.90	5.00	17.65
Mg	0.2-1.6	0	0.00	0.00	0.00	0.00	0.00
Al	91.8-99	0	11.62	10.14	6.78	7.74	7.52
Cr	<0.4	0.20	0.00	0.00	0.09	0.06	0.00
Mn	0.01-1.1	0.25-2.05	0.29	0.25	0.51	0.39	0.28
Fe	0.04-1	97-100	80.97	82.10	88.88	85.89	74.10
Co	0	0	0.25	0.26	0.23	0.24	0.00
Ni	0	0.2	0.13	0.14	0.12	0.13	0.00
Cu	0.01-1.2	0.3	0.27	0.48	0.50	0.54	0.44
O	0.05-0.5	0	0.00	0.00	0.00	0.00	0.00
Ti	0.01-0.25	0	0	0	0	0	0
Si	0.2-1.8	0.15-0.35	0	0	0	0	0
Total	100	100	100	100	100	100	100
Ref/sour	[53]	[53]	EDS	EDS	EDS	EDS	EDS

4.2.1 Characterization of the area in the vicinity of the black area in TN4

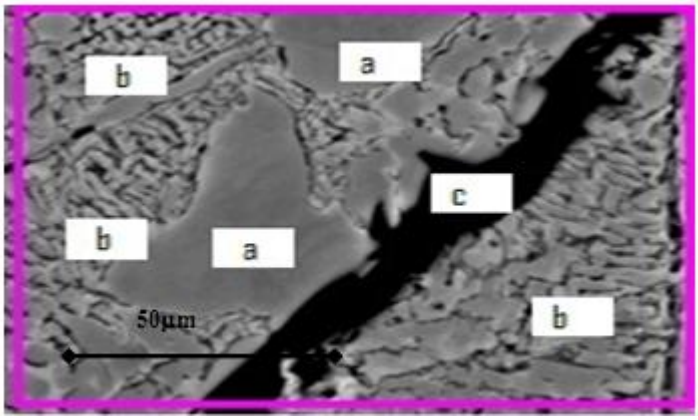

Figure 4.5: Electron microscopy image in the vicinity of the black area of TN4 figure 4.4 showing EDS spots at different locations analysed in table 4.3.

Table 4.3: Chemical composition at locations a, b, c spots of Figure 4.5

	Content of alloying elements in wt%						
	in base materials		At locations or area of the new alloy TN4				
Element	**Al 6061T6**	**Steel 1020**	**Location a**	**Location b**	**Location c**	**Location d**	**Area**
C	0	0.06-1.03	6.29	5.92	95.51	24.79	5.92
Mg	0.2-1.6	0	0.00	0.00	0.00	0.00	0.00
Al	91.8-99	0	11.76	9.53	0.24	7.13	9.53
Cr	< 0.4	0.20	0.07	0.08	0.00	0.00	0.08
Mn	0.01-1.1	0.25-2.05	0.31	0.28	0.00	0.20	0.28
Fe	0.04-1	97-100	80.91	83.24	4.25	67.16	83.24
Co	0	0	0.22	0.18	0.00	0.14	0.18
Ni	0	0.2	0.00	0.16	0.00	0.13	0.16
Cu	0.01-1.2	0.3	0.45	0.61	0.00	0.44	0.61
O	0.05-0.5	0	0.00	0.00	0.00	0.00	0.00
Ti	0.01-0.25	0	0	0	0	0	0
Si	0.2-1.8	0.15- 0.35	0	0	0	0	0
Total	100	100	100	100	100	100	100
Ref/source	[53]	[53]	EDS	EDS	EDS	EDS	EDS

It is seen in Figure.4.5 that there are three different contrasts or phases in TN4. The location c (black area) is essentially made of carbon C (more than 95wt %), almost no aluminum and less than 5wt% Fe and other alloying elements. At locations with a smooth appearance, the aluminum content is above10wt%. The areas b have less aluminum and appear rough. An overview micrograph taken at a lower magnification is shown in Figure 4.4. In figure 4.4 the smooth locations a appear more homogeneous and might be ferrite phase while b locations display lamellae like microstructure, which seems to be pearlite. Black lamellae as discussed in Figure 4.5 contain mostly carbon that results from atomic diffusion from the graphite crucible.

4.2.2 Microstructure of steel-rich samples TN4 at various states

As cast TN4 samples display three phases appearing smooth, rough and dark. Also, black particles or flake like voids are present. When heat treated and water-cooled, small precipitates appear over the surface within the grains. With air-cooling, there are less precipitates and black contrasts are more visible.

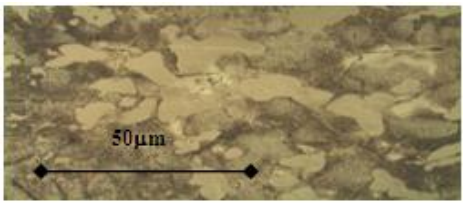

As cast x100

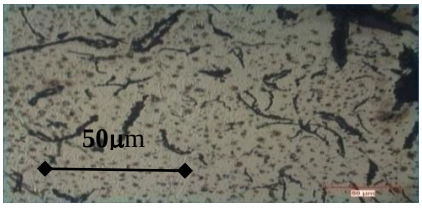

Normalised Water-quenched x400

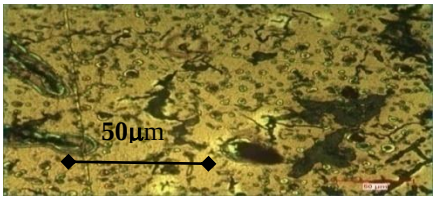

Normalised + air-quenchedx400

Figure 4.6: TN4 as cast and at different heat treatment states

4.3 Diffusion of graphite into the samples

To check the diffusion of graphite into the sample, chemical analysis through SEM-EDX was done for which results are shown below. EDX results (Figure 4.7 a and b) show a high concentration of 57wt% of carbon at sample outer surfaces due to a strong diffusion of carbon atoms from the graphite crucible into the cast samples particularly at very high temperatures during casting, and large inclusions can be seen. The carbon content drops to 3.44 wt% at around 1mm depth towards the centre as seen on the EDX pattern in Figure 4.8a; also there is no inclusion on the micrograph in Figure 4.8b.

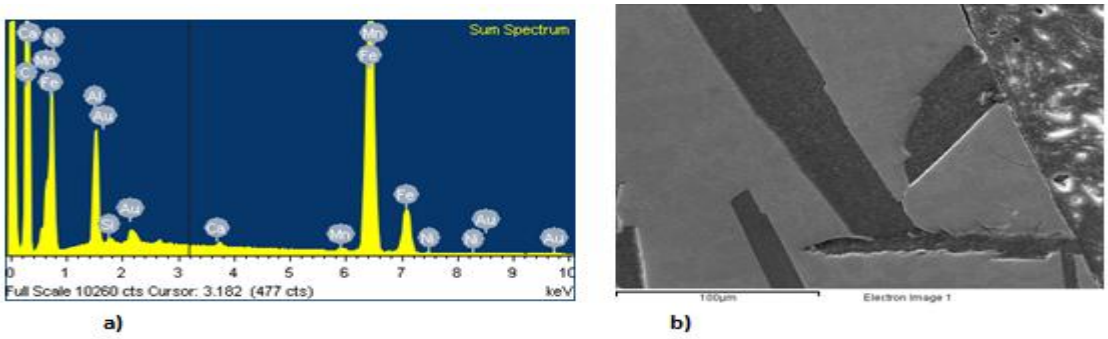

Figure 4.7: a) EDX patterns; and b) SEM micrograph of an area close to the surface of cast TN4 that is in contact with the crucible

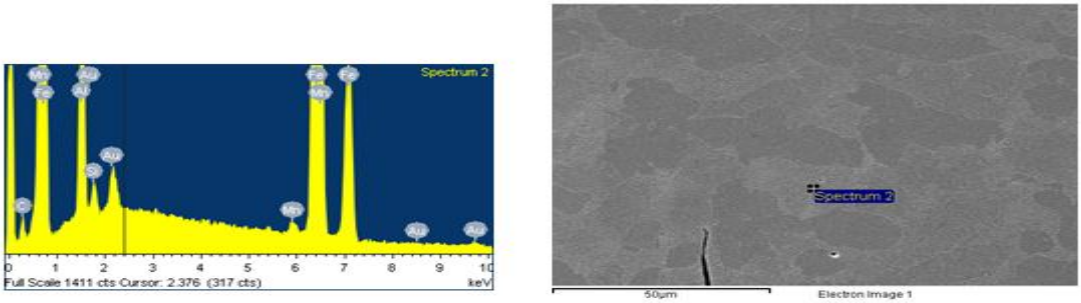

a) b)

Figure 4.8: a) EDX patterns and b) SEM micrograph of an area close to the centre of cast TN4 sample

4.4 Weight reduction for steel-rich samples

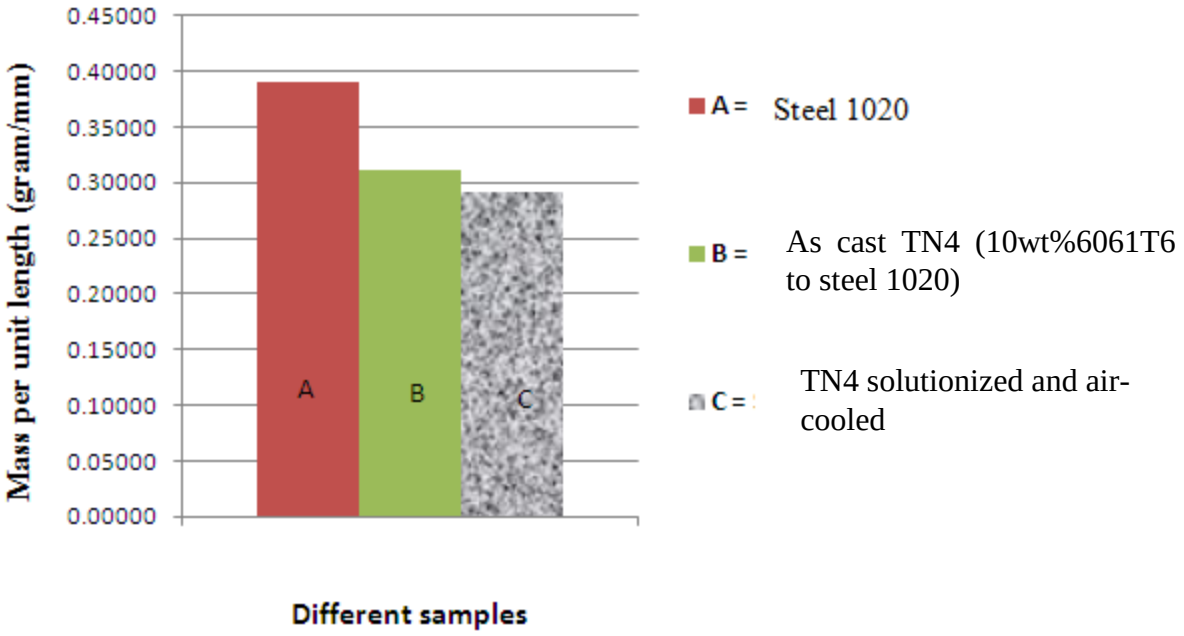

Figure 4.9: Mass per unit length of reference steel 1020 and steel-rich material at different heat -treatment states

In Figure 4.9, it is seen that samples with 10wt% 6061T6 added to 1020 have a mass per unit length of 0.30 gram/mm, which is lower than that of the basic material steel 1020 of 0.38 g/mm. Additional weight reduction seems to occur during heat treatment further reducing to 0.28 g/mm.

4.5 Vickers micro-hardness test results at different heat treatment states

The hardness of the as-cast TN3 is 60 Hv and does not change remarkably after solution heat treatment and ageing.

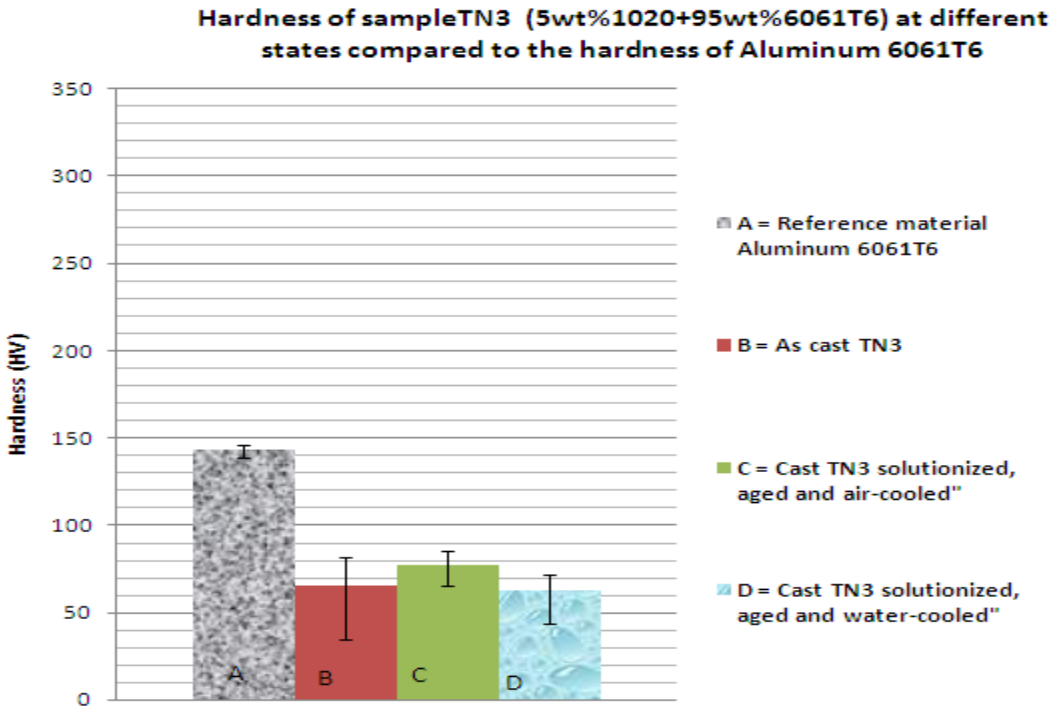

Figure 4.10: Hardness of TN3 at various heat treatment states

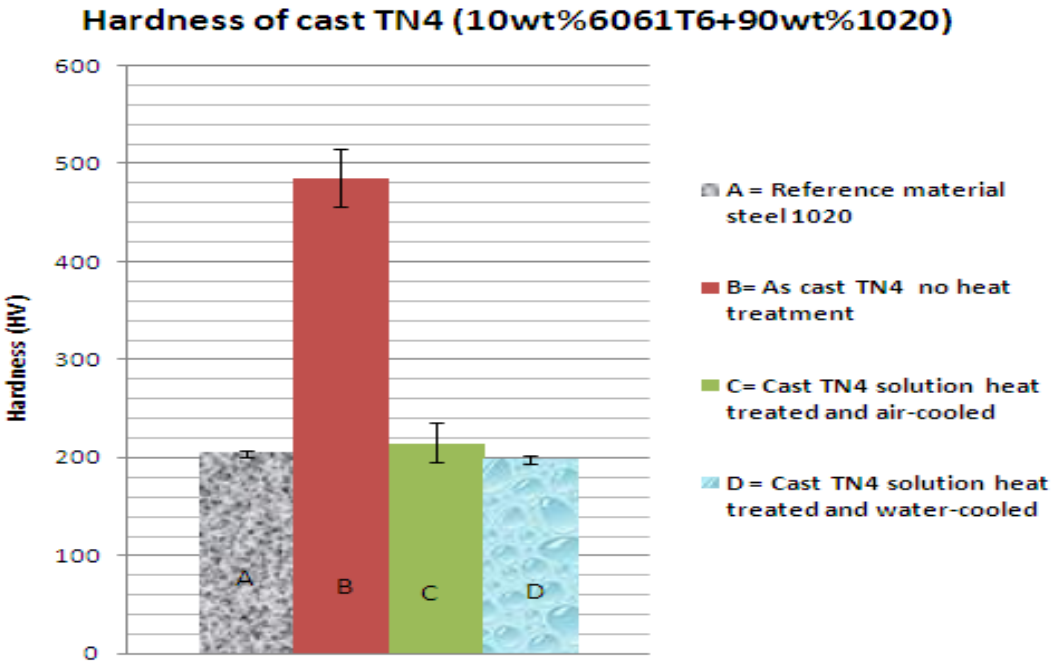

Figure 4.11: Hardness of TN4 at various heat treatment states

In Figure 4.11, it is seen that as cast TN4 has a Vickers' hardness of up to 480 Hv, i.e. more than 2.5 times higher than the hardness of reference material steel 1020 with 200 Hv. After heat treatment and air or water-cooling, the hardness of the casts drops to about 200Hv, which is the hardness of the initial reference material 1020.

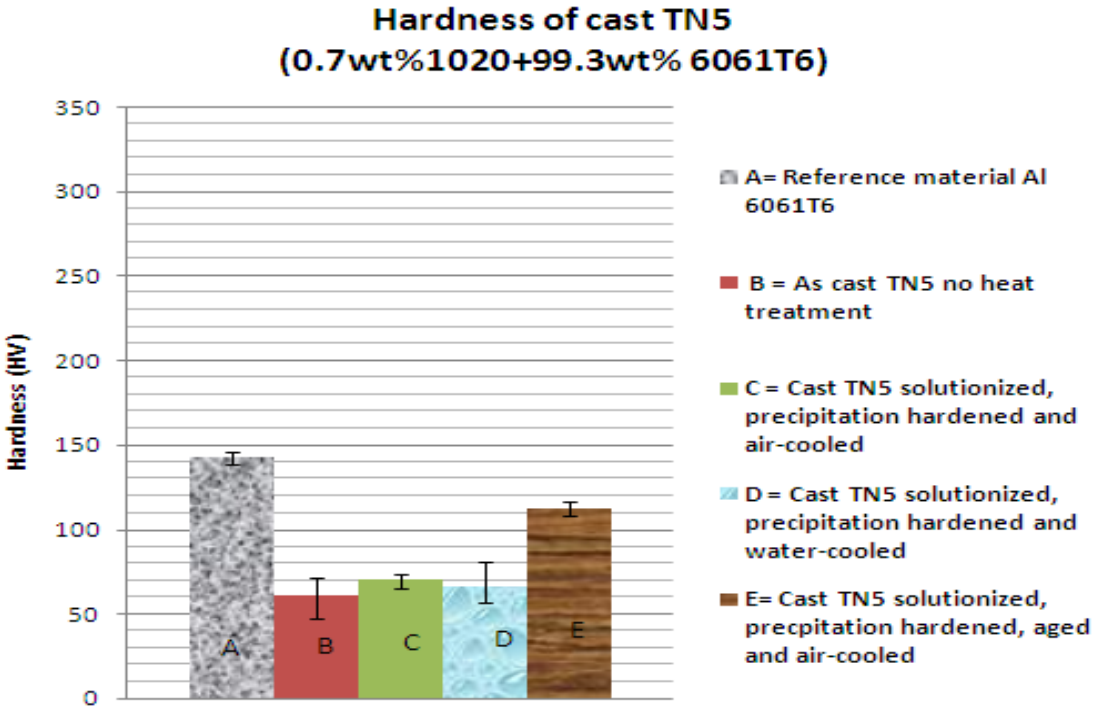

Figure 4.12: Hardness of 6061 T6 and TN5 in various heat treatment states

Figure 4.12 shows a comparison of the hardness of the reference materials 6061T6 and that of aluminum-based samples TN5 at different heat treatment states. The addition of 0.7wt% 1020 to aluminum 6061T6 yields a hardness of 60Hv in the as-cast state which is less than half the hardness of the basic aluminum 6061T6. It remains unchanged after solution heat treatment and when either water-cooling or air-cooling is used. Ageing followed with cooling in air yields an increase in hardness to about 120 Hv, which is still below the initial value for reference 6061T6.

4.6 Wear resistance

The graph in Figure 4.13 shows the mass loss versus wear time for samples TN4 and TN5 at different heat treatment states. The mass losses of aluminum 6061T6 and steel 1020 are also plotted. It can be seen that the mass loss for all materials exhibits a quasi linear relationship with the wear duration. The slope of the plot, which is the wear rate, is highest for aluminum 6061T6 with a value of 0.07 g/minute. TN5 made by addition of 0.7wt%1020 in aluminum 6061T6 shows the next highest wear rate with a value of 0.035 g/minute after solution heat treatment and ageing; this value is only half that of 6061T6, which means two times the wear resistance of the base material 6061T6.

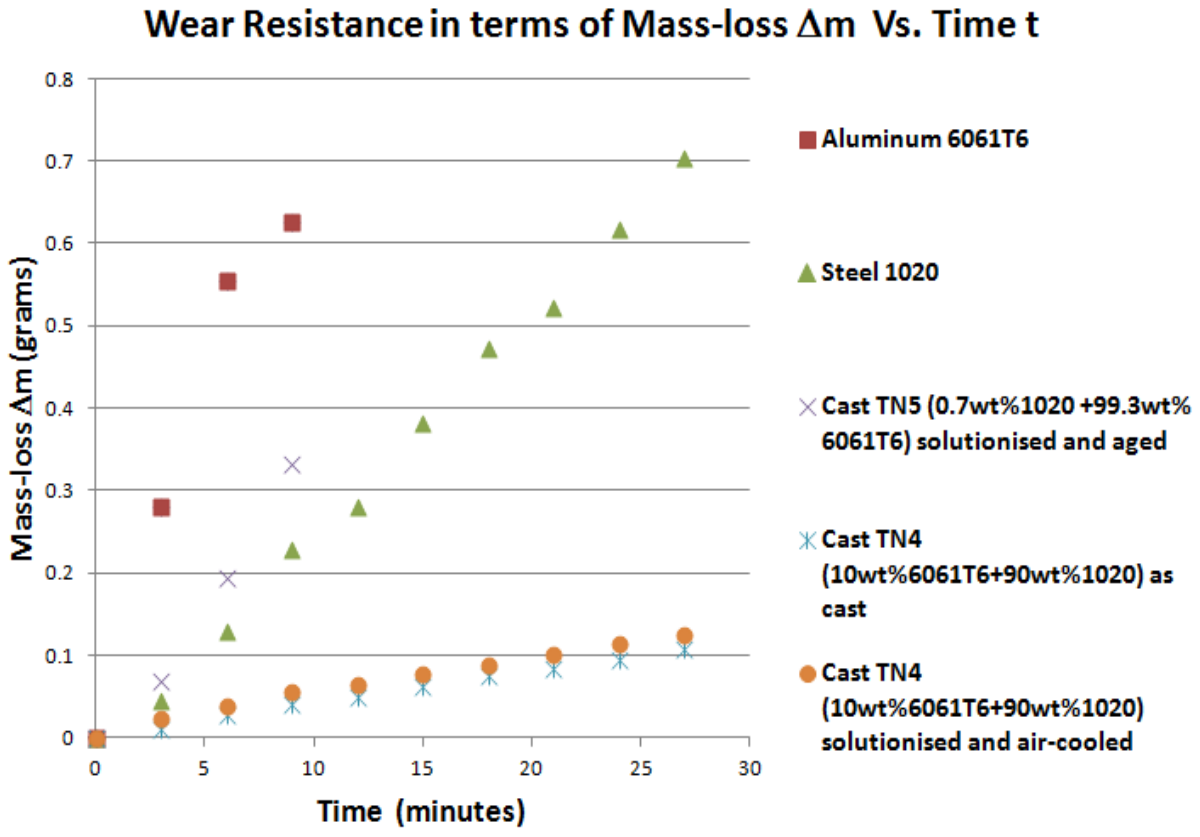

Figure 4.13: Mass loss vs. time of reference materials (6061T6 and 1020) and casts samples at different heat treatment states

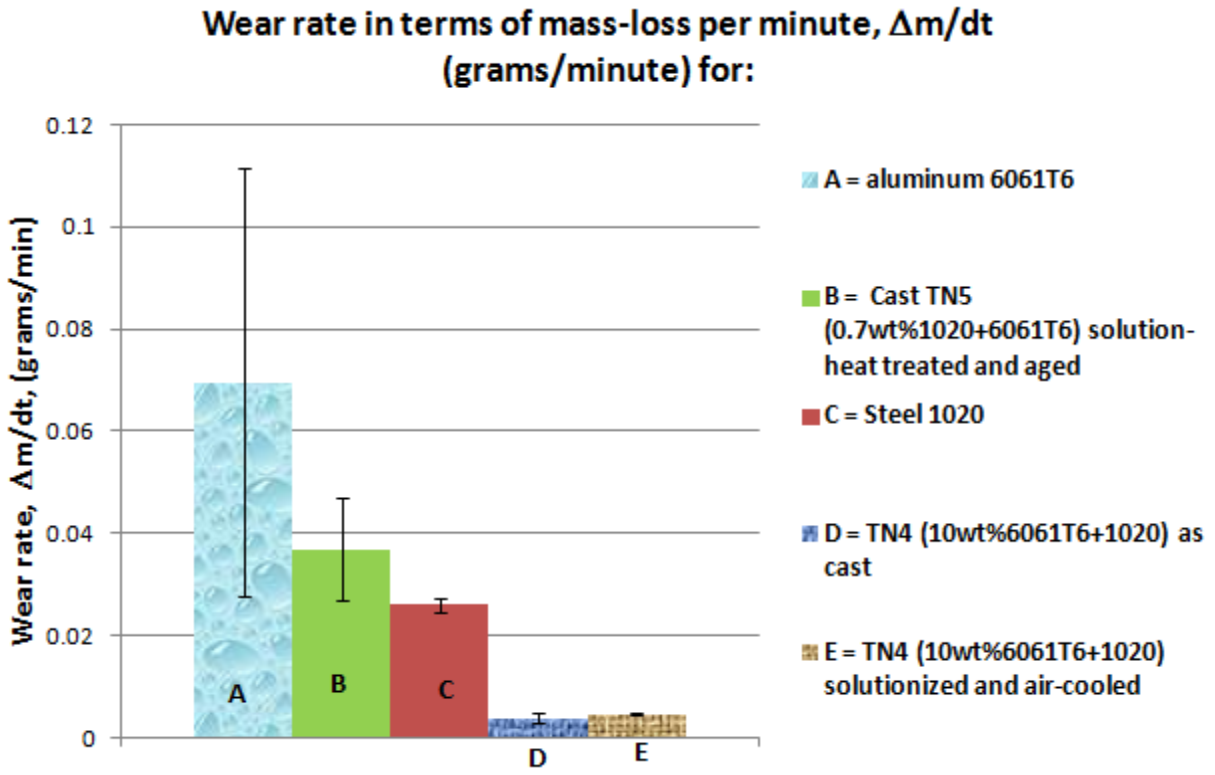

Figure 4.14: Wear rate of reference materials and casts of specified states

TN4 made by addition of 10wt% 6061T6 into steel 1020 has the lowest wear rate in the as-cast state. This high performance of as-cast TN4 practically does not change after solution heat treatment and air-coling. Figure 4.14 and 4.15 show that the wear rate of both the as cast and the heat-treated and air-cooled cast TN4 is less than 0.003 g/minute, i.e. nine times less than that of steel 1020 which is 0.027 g/minute. This means the wear resistance of the new iron-rich 6061T6-1020 mixture is nine times higher than that at the reference steel 1020.

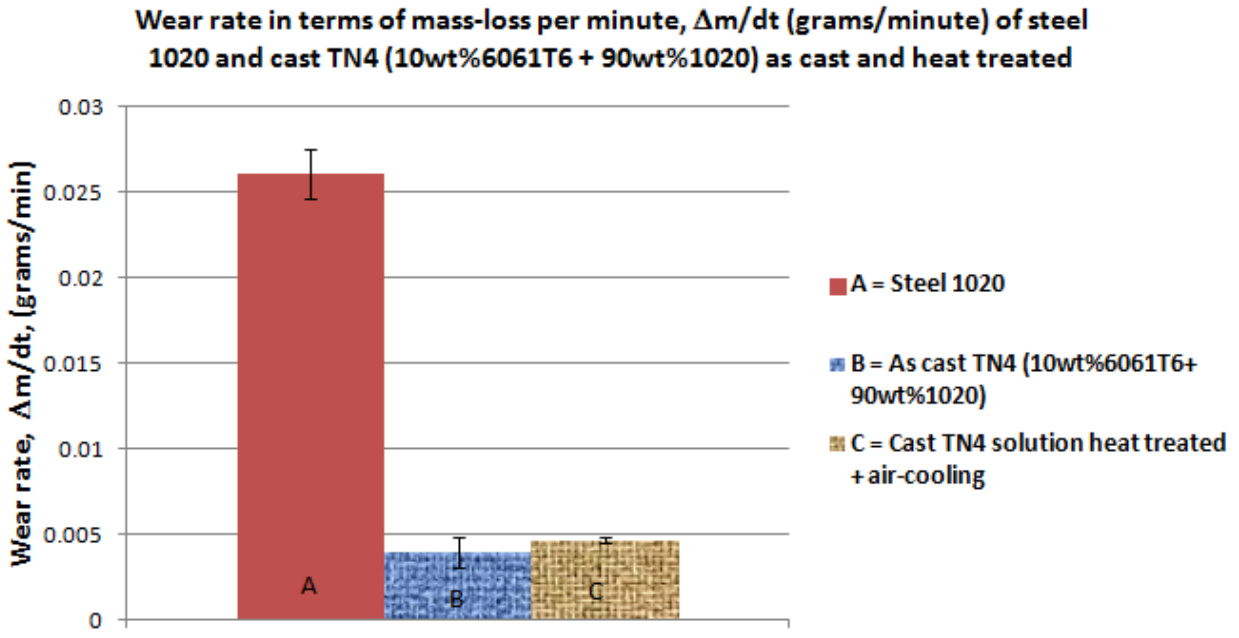

Figure 4.15: Comparison between the wear rate of steel 1020 and cast TN4 at different heat treatment states

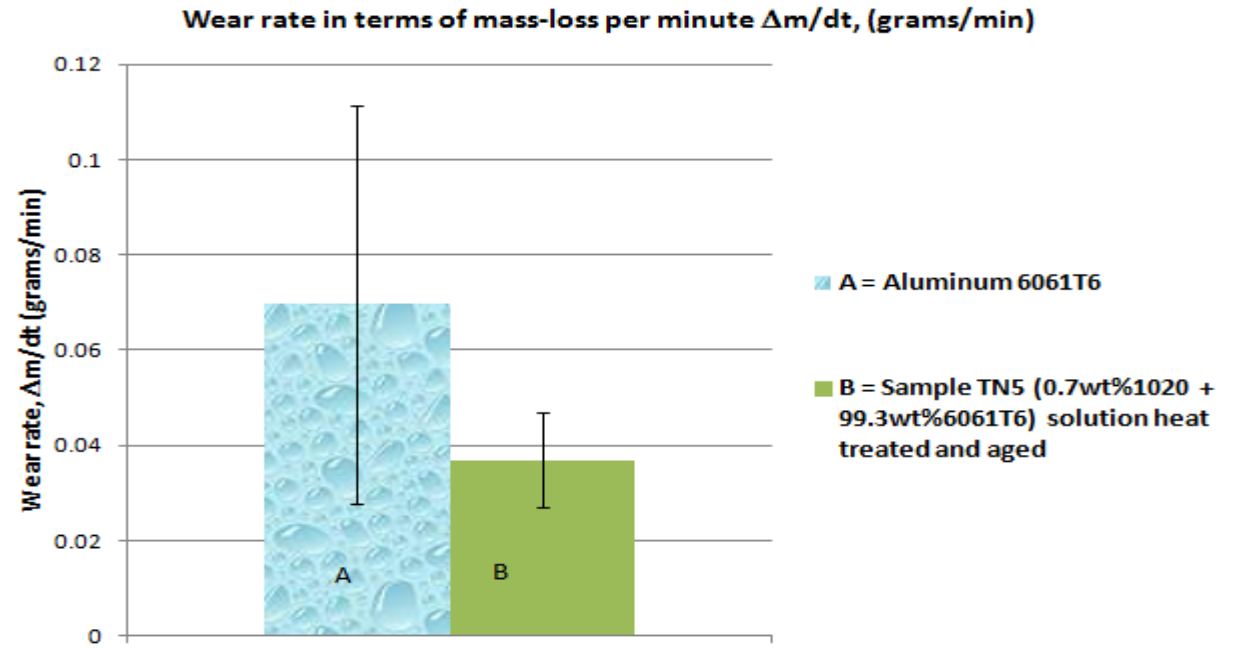

Figure 4.16: Comparison between the wear rate of aluminum 6061T6 and cast TN5 heat treated and aged

It is seen in Figure 4.16 that the wear rate of cast TN5 is lower than that of the reference material aluminum 6061T6. This means that the aluminum rich 6061-1020 mixture has a higher wear resistance than the reference aluminum 6061T6. The other fact in this figure is the huge standard deviation observed in the wear rate of aluminum 6061T6 that exhibits relatively poor consistency. Conversely, for the cast TN5 aged and air-cooled, the standard deviation is small, denoting higher consistency.

4.7 Casting defects

Different casting defects were observed in the cast samples including partial melting and partial mixture, oxidation, macro and micro-porosity.

Figure 4.17: Defects in cast alloy samples: a) unsuccessful melt, b) oxidized sample, c) selective melting of aluminum; steel remains unmolten, d) porosity, e) and f) local melting at the bottom; top section remains unmolten

Some samples did not melt at all (Figure 4.17a). Others melt at the bottom, but melting could not go further, and aluminum pieces got oxidized (Figure 4.17b). The created strong and stable oxide at the aluminum piece surfaces closes and isolates molten aluminum in their interior, thereby preventing mixture and cohesion with neighbouring pieces during casting. In Figure 4.17c, aluminum pieces melted but steel ones did not and are just bonded together by the melted aluminum. It can be seen in figure 4.17d, that unmolten steel pieces and stable oxide scales of aluminum pieces resulted in the lack of internal adhesion, deviations in intended chemical composition as well as porosity and cavities. These phenomena seem to concentrate around steel pieces. Initial aluminum and steel pieces leave large cavities resulting in a loose packing in the mould with low tap density prior to heating. In Figures 4.17e and f, samples melt properly at the bottom and strong mixture of graphite and steel sleeves are seen mostly on steel rich samples.

5 DISCUSSION

5.1 Solubility, microstructure and strength

5.1.1 Aluminum-rich samples

While aluminum maintains the FCC crystal structure until melting, the BCC structure of iron allotropically transforms into FCC above 912^{o}C, then back into BCC above 1394 ^{o}C prior to melting [20]. The atom radius of aluminum is 0.1431 nm and that of steel is 0.1241 nm [20]. The different crystal structures of aluminum and iron at room temperature combined with an atomic radius difference of 13.27% close to 15% suggests a limited solubility of the two elements in each other as can be seen in the aluminum-iron phase diagram in Figure 2.2. The William Rothery rules for solid solution are partially met by aluminum and iron in the Al-Fe system. The iron-aluminum equilibrium phase diagram (Figure 2.2) shows nearly no solubility of Fe in Al on one side, and maximum 12wt% solubility of Al in Fe on the other side.

It is important to recall that instead of pure iron and aluminum of the Iron-aluminum system of the phase diagram Figure 2.2, the materials investigated are steel alloy 1020 and aluminum alloy 6061T6. As seen on their chemical composition in Tables 3.1, 4.2 and 4.3, these materials have several alloying elements which affect microstructures, phases and HT behaviour. Therefore the new alloy is not expected to feature identical phases and microstructures as provided by the iron-aluminum phase diagram figure 2.2. In addition melting is performed in a graphite crucible, which is a carbon isotope; carbon also alters materials behaviour in heat treatment as well as mechanical properties. As a result of the above, microscopic examination of as cast samples TN3 and TN5 with 5wt% 1020 + 95wt% 6061T6 and 0.7wt% 1020 + 99.3wt% 6061T6 respectively show a difference in terms of homogeneity. The SEM image of TN3

(Figure 4.1) displays a clear heterogeneity with varying concentrations of Al and Fe over four identified different contrasts (a, b, c, and d). These differences confirm the excessive solute content far higher than the solubility limit. On the other hand, TN5 is made of 0.7wt% 1020 and 99.3wt% 6061T6. Since aluminum 6061T6 already contains around 1wt% Fe (see Table 4.1), the addition of 0.7wt%Fe brings its total iron content to 1.7wt%Fe. This content is closer to the low solubility limit prescribed by the aluminum-steel equilibrium phase diagram. Indeed, the mixture in TN5 displays greater homogeneity compared to TN3 samples. Remaining on this same side of the phase diagram where aluminum is the base metal (solvent), excess iron is expected to precipitate after ageing as clearly visible in Figures 4.3c and d, resulting in changes in the microstructure. It has been established that, the microstructure has a direct influence on the mechanical properties of metals and alloys. The formed precipitates strengthen the material by impeding the dislocation movement that is primary carrier of plastic deformation at low temperatures. As described in section 3.1, the initial aluminum 6061T6 [55] used in this work was solid solution and precipitation hardened to the maximum strength which justifies its high hardness (140Hv). This initial precipitation strengthening is lost during casting since the initial material is heated above the precipitate dissolution temperature and the melting point of the alloy. Therefore, the precipitates are practically non-existent in the as-cast state resulting in low hardness of the as-cast aluminum rich samples. Figures 4.10 and 4.12 show the hardness of the as-cast aluminum rich samples to be 60Hv, which is lower than the hardness of the reference material 6061T6 of 140Hv. Solutionizing followed by air or water cooling does not improve properties, and the hardness remains below that of the initial 6061T6 aluminum alloy. The aged samples show an increase up to 110 Hv (Figures 4.12), two times the hardness of the as-cast state. Even though this value remains lower than that of the initial 6061T6 alloy, it is an indication of the effectiveness of ageing in improving the strength of aluminum rich alloys made

of recycled aluminum and steel. It illustrates the potential for very high strength of the new alloy, particularly when considering the potential further optimizations.

5.1.2 Steel-rich samples

On the steel-rich side of the Al-Fe equilibrium phase diagram, samples TN4 with the composition 10wt% 6061T6 + 90wt% 1020 meet the first condition of Hume Rothery rules and is below the solubility limit which shall be expected to result in a practically homogeneous single phase solid solution microstructure under equilibrium cooling conditions.

Figure 4.4 shows the microstructure of the as-cast state featuring four different contrasts. As seen in Table 4.2, the chemical analysis of different locations indicates for smooth-like areas (a) a higher percentage of aluminum (11.62 wt%) with Fe concentration of 80.97wt%. b locations are rough with a lower Al content of 10.14wt%. The brighter locations c have the lowest Al content of 6.78wt%. Finally d is less bright than c and has 7.74wt% Al and 85.89wt% Fe. This heterogeneous microstructure is in disagreement with expectations based on the Al-Fe phase diagram and hints to rapid non-equilibrium solidification during cooling of the casts. After solutionising and quenching in water a fifth phase is visible in form of small precipitates that are homogeneously distributed in the material. This clearly shows that additional alloying elements in aluminum and steel alloys as well as impurities can result in a substantial deviation from a homogeneous solid solution microstructure as shall be expected from pure Al-Fe alloys. The air-quenched samples seem to show somewhat larger precipitates with larger interspacing as compared to their water-quenched counterparts. This can be expected as water cools faster than air and therefore provides less time for precipitates to agglomerate and grow, resulting in smaller precipitates in larger numbers. With many, smaller and closer packed precipitates, the movement of dislocations is strongly impeded and plastic deformation strongly restricted. This

results in higher strength and hardness of the water-quenched samples as compare to their air-cooled counterparts. The governing equations for the mechanical strength related to precipitation strengthening are either 5.1 or 5.2. For cutting through particles (small particles)

$$\tau_c = \frac{\rho\,\gamma\,\pi}{b\,L} \tag{5.1}$$

For dislocation bowing (large particles)

$$\tau_b = \frac{G_c}{L-2r} \tag{5.2}$$

Where τ_c , τ_b , $_{L,\,b,\,\gamma}$ and r are critical shear stress for cutting, critical shear stress for bowing, spacing between pinning points, length of burgers vector, surface energy, and practical size (radius for spherical particles) respectively. As the interspacing L of precipitates decreases, the material strength increases for both equations.

Figure 4.11 displays a hardness of the as-cast sample to be 490Hv, about 2.5 times higher than that of the initial steel 1020 that is 200Hv. This high hardness of the as-cast sample is an important achievement of the study, so understanding the mechanism behind it may be very useful. One of the causes of such a high hardness number could be that martensite forms, considering the fact that the BCT (body centered tetrahedral) crystal structure of the martensite has less slip planes compared to the BCC structure of steel 1020 at room temperature. In addition, carbon atoms are at interstitial positions of martensite. It is also known from metallurgical fundamentals that alloying elements, small cross-section, severe quench or very high cooling rate are the main factors that promote martensite formation. The first condition is met as the new material has aluminum 6061T6 added with all its chemical elements mixed together with steel 1020. The second condition is also met as the sample with 12 mm diameter is relatively thin and allows fast cooling. Finally, the cast samples were cooled in air by simply switching off the induction heating system. Considering the very high alloy content in TN4, air-

cooling may be sufficient to allow martensite to form. The other cause of the high hardness may be internal and residual stresses in the as-cast samples due to rapid air-cooling of the liquid. After solution heat treatment and air-cooling, the hardness drops to 210Hv, which is close to 200Hv, the initial value of steel 1020 hardness. This drop results from the fact that the as-cast samples have metastable structures created by non-equilibrium solidification and internal residual stresses. These can easily be lost during subsequent heat treatments as was seen when the hardness dropped from 480Hv to 200Hv.

5.1.3 Hardness and wear resistance

Strengthening effects were extensively investigated using micro-hardness test because of its advantages as stated in section 3.5. Figure 5.1 shows the wear resistance as a function of hardness. As the wear rate changes with the pressure or mass applied on the sample against the disc, a constant mass of 100 grams was used for all tests for consistency.

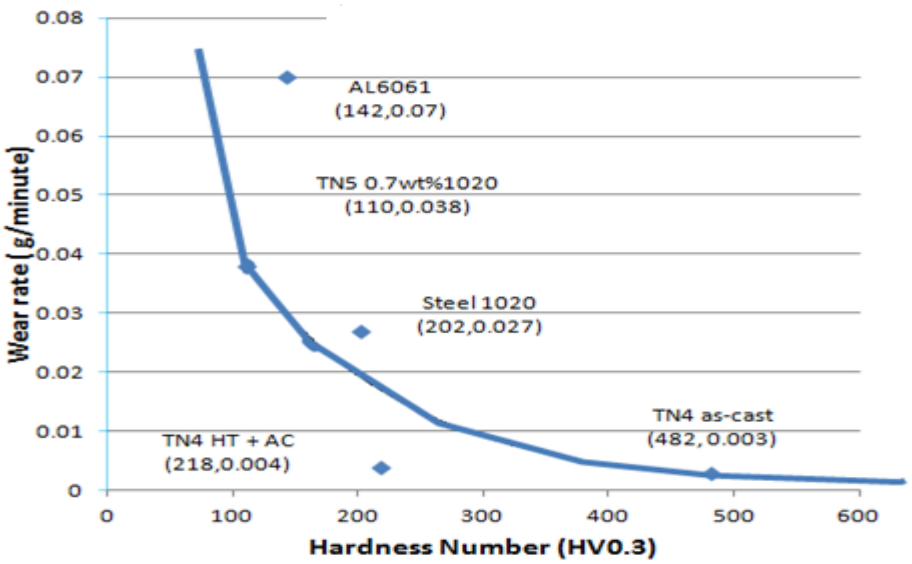

Figure 5.1: Wear rate versus hardness for aluminum 6061T6, aluminum-rich sample TN5 , steel 1020, as-cast steel-rich samples TN4, and TN4 air-cooled.

As explained in Section 5.1, the drop in hardness of the as-cast TN5 to almost half of the 6061T6 value is a result of the dissolution of the initial precipitates during casting. After heat-treatment and artificially ageing, the hardness of the casts improves and the wear rate is two times lower, which means the samples are two times more wear resistant than the reference material Al 6061T6. As explained in section 2.9.1 giving the relation between hardness and fatigue, cyclic stresses cause the disruption of very small areas that bond and break as the surface undergoes friction. It starts with flaws, and when the critical flaw size is exceeded, fracture propagates and the material wears away. From this description, if the softer TN5 alloy has a higher wear resistance than the initial aluminum 6061T6 but remain lower compared to steel 1020, it means that TN5 samples may be deeper indented by particles but they deform only plastically or elastically rather than cracking, losing material or wearing out. This hints to higher fracture toughness and potentially higher fatigue resistance

On the other side, the steel-rich TN4 samples either as-cast or heat treated display higher hardness and wear resistance compared to the base material 1020 as seen in Figures 4.11, 4.14 and 4.15. However, the relationship between hardness and wear resistance does not seem linear. For example, the as-cast state has a hardness number of 480 Hv and a wear rate of 0.003 g/min while the heat-treated and air-cooled state has a hardness of 218 Hv and a wear rate of 0.004 g/min. This means more than double the hardness leads to only 25% increase in wear resistance. This again hints to a much higher toughness and ductility of the heat-treated steel rich TN4 samples. The base steel 1020 has a hardness of 202 Hv not too far from that of the water-cooled and air-cooled samples, but displays a wear rate of 0.027 g/minute, which is about 9 times higher, meaning a 9 times lower wear resistance. Steel alloy 1020 and TN4 HT+AC have almost the same hardness but the latter has a lower wear rate (wear rate of 0.004 g/min for TN4, 0.003 g/min TN4 + air-cooling, and 0.027 g/min for 1020) meaning a higher wear resistance.

Following the same trend, solutionized and aged TN5 has a wear rate of 0.038 g/min compared to 0.07 g/min for aluminum 6061T6 while having nearly the identical hardness. It can be concluded that toughness is a major factor for wear resistance besides the hardness as already known from literature.

5.2 Weight changes and weight reduction

High strength-to-weight ratio is one of the main criteria of modern design for structural materials. High strength-to-weight ratio allows reducing centrifugal stresses in rotating components and reduces energy consumption as well. The specific hardness and wear resistance are the hardness and wear resistance of an alloy divided by its density. On the steel rich side, the mass of the cylindrical wear test samples with an identical volume of 803.84 mm^3 are 6.26 grams for steel 1020, and 4.70 grams for TN4 (10wt% 6061T6 + 90wt% steel 1020). This weight reduction is in accord with the rule of mixture as the added aluminum is much lighter than the solvent steel 1020. Using Equation 2.8 and considering the alloy TN4 made of 10wt% aluminum 6061 (density $\rho_a = 2.7$ g/cm^3) and 90wt% steel 1020 (density $\rho_s = 7.9$g/cm^3), the density of TN4can be estimated as follows:

$$\rho = \frac{100}{\frac{10}{\rho_a} + \frac{90}{\rho_s}} = \frac{100}{\frac{10}{2.7} + \frac{90}{7.9}} = 6.75\ g/cm^3$$

The percentage of weight reduction can then be estimated as

$$\frac{7.9-6.75}{7.9} * 100 = 14.55\%$$

The discrepancy between the measured and calculated weight reductions can be rationalised by some porosity in the cast samples combined with estimate and measurement errors. The following percentage of weight reduction can be computed using the percentage of the mass

difference between wear test samples of the base steel 1020 (6.26 g) and as-cast TN4 (4.70g) from equation (3.3).

$$\frac{6.24-4.79}{6.24} * 100 \ = 24.9\% \ \sim 25\% \text{ weight reduction}$$

This result reflects the difference in specific-mass seen in figure 4.9.

5.3 Oxidation and effect of argon protection

Aluminum and steel spontaneously react with oxygen in air to form an oxide scale. The oxidation rate increases with temperature and is particularly strong at the high temperatures needed to melt the metals. The issue of oxidation was found to be less critical for steel than for aluminum; steel could be molten even in air without argon protection. This can be rationalised by the difference in thermal stability of iron oxide and aluminum oxide. In fact, in contrast to the strong, stable and dense Al_2O_3 scale at the surface of aluminum alloy particles, Fe_2O_3 is less thermally stable and ruptures at the relatively high melting temperature releasing the molten core. Therefore, mixture and cohesion of neighbouring particles to form a solid cast is possible. The formula below illustrates the typical oxidation reaction of metals:

$$aM + \frac{b}{2} O_2 \ \rightarrow M_a O_b \tag{5.3}$$

Where M and O represent metal and oxygen atoms respectively; a and b represent the ratios of the atoms or mol of metal and oxygen, respectively, involved in the above stoichiometric reaction. The use of argon flow helped to limit oxygen from reaching the metal surface in order to limit oxidation. In the case of optimal argon protection, the metal surfaces would be in contact with only argon, which would completely prevent chemical reactions since Argon is inert. In addition, the relatively large argon atoms tend not to diffuse into the melt. The mechanism of oxidation protection by argon flow from the top relies on the fact that the density of argon is

much higher than that of air; the atomic weight of argon is 39.94 g/mol while that of oxygen is 15.99 g/mol. When argon flows into the crucible, it pushes the air out and replaces it from the bottom up thanks to its greater weight. This higher density of argon may also explain why melting and sample purity was found to be best at the bottom of the cast samples.

During heating under inert environment, Aluminum would melt first as its melting temperature (660^{o}C) is reached before that of steel (1530^{o}C). 1530^{o}C is still under the aluminum boiling temperature allowing the aluminum to remain liquid during casting. Therefore, complete solubility and mixture is possible in the liquid state. Because of the combined effect of diffusion, convection, conduction, and the stirring effect of the magnetic field in the molten metal characteristic of induction heating homogeneous samples result.

5.4 Analysis of main casting defects

As seen in Figure 4.17, the use of induction heating, graphite mould, and extremely simplified test setting lead to some characteristic defects. First, continuous argon flow does not prevent oxidation completely, particularly at the surface of initial aluminum pieces short before melting. Al oxidation results in a strong and stable Al_2O_3 oxide scale that enclosed and isolated molten aluminum in their interior thereby preventing mixture and cohesion with neighbouring pieces during casting. Secondly, aluminum and steel pieces leave large spaces between each other resulting in a loose packing in the mould with low tap density prior to heating. Therefore, the load collapses upon melting of the bottom section and the still solid pieces on top scratch the relatively soft graphite mould as they fall, removing graphite particles that remain as inclusions in the final cast. Third strong diffusion of carbon into the molten liquid results in high carbon contents in surface areas of the casts. Finally, some steel pieces that remained unmolten due to their much higher melting point and stable oxide scales of aluminum pieces resulted in some

cases in the lack of internal adhesion, lack of appropriate mixture, deviations from the intended chemical composition as well as porosity and cavities due to bridging around the solid particles.

5.5 Effect of current density, magnetic field distribution and load location

It was observed that all samples melt properly at the bottom of the crucible, which can be partially explained by the better argon protection there. As discussed above, the higher density of argon compared to air leads to a higher concentration of argon at the bottom of the crucible and therefore to a more inert environment, less oxidation and ultimately better melting, mixing and solid formation upon cooling. Uneven concentration of the magnetic field along the coil axis also contributes to uneven melting along the cast sample length. Based on the above features of induction heating, it is interesting to recall that, during melting, changes were observed in power, voltage, current density and frequency as the load (crucible filled with metal pieces) was lowered or lifted. It is by so doing that melting of the entire sample length was achieved and most of the defects could be avoided. Zinn also suggested this practice [47] as it helps to achieve maximum eddy current density locally throughout the sample as it is moved through the magnetic field of the heating coil.

5.6 Influence of power supply, impedance matching, tuning and power transferred

5.6.1 Required melting power of aluminum-steel alloy samples

Assumptions

For simplicity purposes, parameters of 6061T6 are used for Al rich samples and those of steel 1020 were used for steel rich samples. From the thermodynamics fundamentals, it is known

that, for a material to melt, phase changes occur and lead to changes in specific heat and resistivity. Additionally, melting takes place at constant temperature where the latent heat is used.

The following additional assumptions are made:

1) specific heat and resistivity are considered constant and room temperature values are used. The target temperature is the melting point where all the material is heat up to this point (heating power P_H).

2) The latent heat of fusion of aluminum–rich samples and steel-rich sample are considered equal to that of aluminum 6061T6 and steel 1020 respectively; each material will melt under the melting power P_M

3) As steel is ferromagnetic and changes its relative permeability from 100 to unity at the Curie point of 783^{o}C, two cases. The energy needed to heat until Curie temperature with magnetic permeability and the energy needed to heat from Curie temperature to the melting point (1530^{o}C) with non magnetic properties.

In this thesis, the crucible used is made of graphite, which is nonmagnetic but conductive. This conductivity adds some power loss, thus increases the power requirement due to Joule effect.

5.6.2 Power required

The formula to determine the power required for heating was established by S. Zinn [60] as follows:

$$P = P_1 + P_{rad} + P_{conv} + P_{coil} \tag{5.4}$$

Where P is the total power needed from the AC power source to the induction coil; P_1 is the power needed to melt the material; P_{rad} is the power loss from the workpiece due to radiation;

P_{conv} is the power loss from the work piece due to convection; and P_{coil} represents power losses in the coil due to joule heating.

- ***Power lost by convection P_{conv}***

The heat power P_{conv}, lost through convection is very small and can be neglected.

- ***Power needed to melt the material P_1***

For melting, the absorbed power depends on the required temperature rise ΔT and the total weight to be heated per unit time W. Therefore, P_1 used to melt the load is

$$P_1 = WC\Delta T + L\,.\,M \tag{5.5}$$

Where W = Volume (cm^3) x volumic mass (kg/cm^3) / time (second), L is the latent heat of fusion of each material and M is the mass of the material to melt per second.

$$W\left(kg/_{sec}\right) = \frac{\pi\, r^2 L\,.\ volumic\ mass}{time} \tag{5.6}$$

r = 0.6 cm is the sample radius; L = 8 cm is the sample height; and time = 600 seconds (10 minutes) is the total time the samples were held in the heating coil at full power. The volumic mass of aluminum is $2.71\text{x}10^{-3}$ kg/cm^3 and that of steel is $7.8\text{x}10^{-3}$ kg/cm^3.

Table 5.1: Computation of power required to melt the materials

Parameter	Aluminum-rich sample	Steel-rich sample
πr^2L.Vol mass (kg)	$24.507*10^{-3}$	$70.989*10^{-3}$
W (kg/second)	$0.0408*10^{-2}$	$0.1183*10^{-2}$
C (J/kg-^{o}C)	896	486
ΔT (^{o}C)	640	1510
$P_H = W\,.\,C.\Delta$T (watt)	233960 x 10^{-3} = 233.9 watts	868156.38 *10^{-3} = 868.15watts
M (cf above W in kg/s)	$0.0408*10^{-2}$	$0.1183*10^{-2}$
L *(kJ/kg.sec)* [62]	398	272
$P_M(kW) = L.M$	0.1624 = 162.4 watts	0.3218 = 321.8 watts
$P_1 = P_H + P_M$	396.3 watts	1189.95 watts

- ***Power loss by radiation P_{rad}***

The radiation loss is

$$P_{rad} = Ae\sigma\ (T_2^4 - T_1^4\ ) \tag{5.7}$$

Where, e is the emissivity of the workpiece surface (0.1 to 0.2 for aluminum and 0.80 for steel) [57]. For the present estimation, 0.2 is used for aluminum. σ is the Stefan-Boltzmann constant; T_2 and T_1 are the work piece target and ambient temperature respectively, and A is the surface area of the workpiece.

$$A = \pi\frac{d^2}{2} + \pi d.L \tag{5.8}$$

d = $12x10^{-3}$ m and l = $80x10^{-3}$m; A = (226.08+ 3014.4) $x10^{-6}$ =$3240.48x10^{-6}m^2$

Table 5.2: Composition of power loss through radiation

Parameter	Aluminum-rich sample	Steel-rich sample
A(m^2)	$3240.48 * 10^{-6}$	$3240.48 * 10^{-6}$
E	0.2	0.80
σ ($W/m^2.K^4$) [61]	$5.67 * 10^{-8}$	$5.67 * 10^{-8}$
T_2 (^oK)	953	1823
T_1 (^oK)	313	313
$(T_2^4 - T_1^4\ )$	$8.15 * 10^{11}$	1.10349E+13
$P_{rad} = Ae\sigma\ (T_2^4 - T_1^4\ )$	29.96 watts	1622.8 watts

- ***Power loss through Joule effect in the coil P_c***

Power loss by Joule effect in the coil is

$$P_c\ =\ P_{coil}\ =\ I_c^2.R_c \tag{5.9}$$

R_c, the resistance of the heating copper coil can be derived from the electrical efficiency η as follow:

$$\eta = \frac{R_{eq}\, I_C^2}{R_c\, I_C^2 + R_{eq}\, I_C^2} = \frac{R_{eq}}{R_c + R_{eq}} \tag{5.10}$$

From which R_c is derived as follow

$$R_c = R_{eq}\,\frac{1-\eta}{\eta} \tag{5.11}$$

The efficiency η for a helical coil and cylindrical work piece is given in Table 2.4 and is 0.80 for steel and 0.60 for aluminum. From equation 2.15, R_{eq}, the equivalent resistance of coil plus load is:

$$\mathrm{R_{eq}} = \frac{\rho\pi a}{A_S}\, K_{R_2} N^2 \tag{5.12}$$

Where the sample diameter is a = $12\text{x}10^{-3}$ m, and the cross section of the sleeve

$$A_S = d.w \tag{5.13}$$

with d being the reference depth assumed equal to the radius of the workpiece since the entire cross-section is to be heated up to melting. Therefore d = 6 x 10^{-3} m and w is the width of the sleeve and can be estimated by dividing the sample length (80mm) by the number of turns N (8) as: 80 mm/8 = 10 mm = 10^{-2}m; this yields A_S = 60 x 10^{-6} m^2.

The resistance factor K_{R2} is found from Figure 2.6a (literature review); the ratio a/d (diameter /depth penetration) is 12/6 = 2 making K_{R2} = 0.2

$$\mathrm{R_{eq}} = \rho\frac{\pi a}{A_S}\, K_{R_2} N^2 = \rho * \frac{\pi .12 .10^{-3}}{60\ \mathrm{X}10^{-6}} 0.2 * 8^2 = \rho * 8038.4 \tag{5.14}$$

For experiment, the current displayed for aluminum rich samples is 50 A and that for steel rich samples is 60 A.

Table5.3: Composition of power Pc lost through Joule's effect in the copper heating coil

Parameter or Formula	Aluminum-rich sample Ic = 50A	Steel-rich sample Ic = 60A
Resistivity (ρ) (Ω.m) x 10^{-6}	3.7 * 10^{-2}	0.16
$\frac{\pi a}{A_S} K_{R_2} N^2$	8038.4	8038.4
$\rho \frac{\pi a}{A_S} K_{R_2} N^2$	2.9742 * 10^{-4}	1.28614 * 10^{-3}
$\frac{1-\eta}{\eta}$	0.6666	0.25
$R_c = R_{eq} \frac{1-\eta}{\eta}$	1.9826 * 10^{-4}	3.215 * 10^{-4}
P_C (watt)	0.496 watt	**5.16 Watt**

- ***Power loss through Joule effect in the graphite crucible P_G***

To estimate the joule effect of the graphite crucible, the emptied crucible is assumed to be the workpiece and heated in the induction coil. Therefore, the equivalent resistance of the crucible is computed from Equation 2.14 (literature review), and P_G is found using the formula

$$R_G = R_{eqG}.I_C^2 \tag{5.15}$$

$$R_{eq_G} = \frac{\rho.\pi.a}{A_S}.K_{R_2}.N^2 \tag{5.16}$$

Where, as defined earlier, the diameter a = 16 x 10^{-3} m (outer diameter of the crucible)

with d, the reference depth, now assumed equal to the thickness T of the crucible wall since the heat should go through the crucible to reach the material.

Therefore, d = 2 x 10^{-3}m; w is the width of the sleeve = 10^{-2}m as also defined earlier.

This yields: A_S = 2 x10^{-3} x 10^{-2} = 2x 10^{-5}m^2.

K_{R2} is found from Figure 2.6b (literature review); the ratio T/a (thickness/diameter) = 2/16 = 0.125 and a/d = 16/2 = 8 making K_{R2} = 1.2

$$\frac{\rho\pi a}{A_S} K_{R_2} N^2 = \rho \frac{\pi .16 .10^{-3}}{2 .10^{-5}} 1.2 * 8^2 = \rho . 1929.216 * 10^2 \qquad (5.17)$$

Table 5.4: Power loss through Joule effect in the graphite crucible

Parameter or Formula	Graphite (I=50 A)	Graphite (I=60 A)
Resistivity (ρ Ω.m) * 10^{-8}	10	10
$\frac{\pi a}{A_S} K_{R_2} N^2$	1929.216 *10^2	1929.216 *10^2
$R_{eq_G} = \rho \frac{\pi a}{A_S} K_{R_2} N^2 (\Omega)$	19292.16 *10^{-6}	19292.16 *10^{-6}
$P_G = R_{eq_G} I_C^2$	48.23	69.45

Power Balance

Summing the four power requirement contributions P_1, P_{rad}, P_{coil} *and* P_G yields a coarse estimate of the total power required for samples to be molten. As seen in Table 5.5, in both cases, the estimated total power requirement is lower than the maximum power output of the TUCKER induction machine, which is 3000 watts (3 kW). The power needed for steel-rich samples is very close to the output, which partly explains difficulties encountered for melting them.

Table 5.5: Overall power required for melting process of aluminum-rich and steel-rich samples

Power required	Aluminum-rich samples	Steel-rich samples
P_1	396.3 watt	1189.95watt
P_{rad}	29.96 watt	1622.8 watt
P_{coil}	0.496 watt	1.16 watt
P_G	48.23 watt	69.45 watt
Total power requirement (watt)	475	2883.4
Power output (watt)	3000	3000

6 CONCLUSIONS

Investigating the Philosophy for Recycling, Alloying–Recycling, Al-Fe based alloys are successfully produced using induction melting of existing Al 6061 T6 and steel 1020 rods, casting using graphite crucibles and in some cases solution and aging heat treatments. The new alloys showed the following microstructure and properties:

1) The Fe rich alloy TN4 with 10wt% 6061T6 and 90wt% 1020 has primarely a solid solution microstructure made of ferrite (α). In contrast, the microstructure of aluminium rich samples TN3 with 5wt% 1020 and 95wt% 6061T6 and TN5 with 0.7wt% 1020 and 99.3wt% 6061T6 have primarily a solid solution structure and some precipitates particularly after ageing heat treatment.
2) The hardness of the as-cast TN3 and TN5 are 65 Hv and 60 Hv respectively, which is about half the initial hardness of 6061T6 that is 140 Hv. However, after precipitation hardening for 4 hours, the hardness of TN3 and TN5 do not change when water-cooled, but show a slight increase to 110Hv when aged and air-cooled, and the wear rate is appproximately 0.038 g/min while that of 6061T6 is 0.07 g/min. This means an improvement in wear resistance by about a factor two in the new alloys.
3) For TN4, the hardness in the as-cast state is 480 Hv which is 280 Hv above the hardness of the initial steel 1020. This relatively high hardness value is probably due to solid solution strengthening, internal residual stresses, inclusions and potentially martensite formation in the as-cast TN4 alloy. The hardness decreases after solutionizing to 208 Hv for air-cooling and to 200 Hv for water quenching. The wear rate of solutionized TN4 is 0.003 g/min for air cooling and 0.004 g/min for water quenching, which is about nine times lower than the wear rate of the initial steel 1020

that is 0.0227 g/min or nine times more wear resistant. This means again a substantial improvement in wear resistance of the new alloy.

4) In addition to showing a higher wear resistance, the iron rich alloy TN4 is lighter and shows a weight reduction of about 25% with respect to the initial steel 1020.
5) The main defects observed in the cast samples were partial melting or mixing and macro-voids primarily due to limited heating power or poor tuning of the available induction system as well as oxidation. In some cases, oxidation and micro-porosity were observed due to deficient protection using continuous argon flow.

Overall, the current work successfully demonstrates the feasibility of a new recycling philosophy (Alloying-Recycling) for aluminum alloys and steels. This new philosophy favours the production of mixture alloys rather than attempting to re-produce alloys similar to the primary ones in microstructure and properties. In contrast to often-lower grade alloys resulting from the latter approach, the new philosophy shows the potential of resulting in a new class of materials with properties even better than those of primary materials and potentially higher strength and stiffness-to-weight ratios which are becoming the new norm and requirement in structural design.

7 OUTLOOK

The current thesis has focused on the potential of mixture alloys made of recycled aluminum and steel in contrast to the standard approach termed “closed loop”, that aims at producing recycled alloys with composition, microstructure and properties as close as possible to the initial primary alloys. The new approach may help relax requirements for cleaning, sorting and purification of recycled materials, which usually lead to high recycling costs. However, the current thesis focuses only on metallurgical aspects since the process of recycling as such is scientifically and technologically well advanced. Still, a full range of critical aspects needs to be addressed in future research:

First, the properties of the resulting Al-Fe alloys shall be investigated as a function of contamination in order to assess the impact of impurities. The degree of tolerance of impurities in the new alloys shall be investigated as well as their property changes as a function of impurity type and content.

Second, the casting procedure needs to be improved. This can be achieved by changing the mould material in order to eliminate carbon contamination or simply by substantially increasing the sample size and machining the contaminated sample surface. Furthermore, a higher power induction system is required to overcome difficulties in melting particularly steel. In addition, a better way to protect the cast load from oxidation shall be found since argon flow does not seem to provide sufficient protection. Electrical short circuiting issues came out during the experimental work; a clay lining was designed for thermal and electrical insulation and was very useful. It might be interesting to investigate further the crucible design. Another suggestion

is the conception of a remote control system to handle and move the sample (workpiece and crucible) during melting for optimal exposure to the magnetic field.

Third, vacuum melting seems most appropriate for improving protection from oxidation; however, it requires huge investments and maintenance service. Therefore, conception and design of a crucible, vacuum tube or containers that consider and address cost consideration is required.

Fourth, for each sample, the crucible was broken due to difficulties to remove the cast. Ways to recover the sample without destroying the crucible could further cost through re-use of crucibles. Additionally, material loss due to oxidation from the outer surface of the crucible during heating weakens this molten metal container, which can be hazardous due to potential leakage of the molten metal. On the inner face, loss of crucible material leads to inclusions and contamination. Therefore, it is suggested to investigate alternative crucible material, design or treatments.

Fifth, further tests shall be performed on the new alloys in order to completely characterise their mechanical, corrosive and thermal properties. The actual recycling process, the effect of non-metallic impurities shall be investigated in future works. Also, the casting and heat treatment processes need to be improved.

8 REFERENCES

[1] M. Cohen, Advanced Materials & Processes, **Vol. 147**, No3, pp. 70, No 2, pp.38, 1995, Copyright 1995 by ASM International.

[2] http://en.google.asf/The American Foundry Society, Technical Department, Metals casting design, retrieved July 15, 2011.

[3] Anders Damgaard et al., Accounting of greenhouse gases and global warming contributions, Technical University of Denmark, Kongens Lynby, Denmark 2009.

[4] European Commission, Integrated Pollution Prevention and Control, Bruxelles Belgium, 2001.

[5] M.P. Thomas and A.H. Wirtz, Alcan Aluminum Limited, Montreal, Canada and Deuschland GmbH, Eschborn, Resource conservation and recycling, **10,** 1994 pp.193-204, Germany 1994.

[6] http://www.doitpoms.ac.uk/ttplib/recycling-metal, Doit website's, University of Cambridge, Recycling of metals, retrieved 7/04/ 2008.

[7] Sérgio Francisco dos Santos, José de Anchieta Rodrigues (2003), Correlation between Fracture Toughness, Work of Fracture and Fractal Dimensions of Alumina-Mullite-Zirconia Composites. Materials Research **6** (2)' pp. 219–226.

[8] H. Amini Mashhadi et al., Recycling of aluminum alloy turning scrap via cold pressing and melting with salt flux, Journal of Materials Processing Technology **209,** 2009, pp. 3138 – 3142.

[9] G. O. Verran, U. Kurzawa, An experimental study of aluminum can recycling using fusion in induction furnace, State University of Santa Catarina Brazil, Science Direct Resources Conservation & Recycling, **vol. 52,** 2008, pp.731-736, Brazil 2007.

[10] H. Puga et al., Recycling of aluminum swarf by direct incorporation in aluminum melts, Journal of Materials Processing and Technology **209,** 2009, pp.5195-5203.

[11] Jorge Alberto Soares Tenario et al., Effect of salt/oxide interaction on the process of aluminum recycling, Polytechnic School, University of Sao Paulo, Journal of Light Metals, **vol. 2,** 2002, Sao Paulo Brazil, 2002.

[12] J. F. Knott, Metallurgical aspects of toughness of engineering alloys, Pembroke Street, Cambridge CB2 3QZ, U.K. 1981.

[13] B. Liu, Y. F. Zheng, Effects of alloying elements (Mn, Co, Al, Sn, B, C, and S) on biodegradability and in vitro biocompatibility of pure iron, State Key Laboratory for Turbulence and Complex System and Department of Advanced interdisciplinary Studies, Peking University, Beijing **100871**, People's Republic of China.

[14] Michael B. Bewer, The recycling of metals-II non ferrous metals, Conservation Recycling **vol**. **1,** pp. 137-147, Pergamon press MA02139, USA.

[15] J. H. Wesbrook and R. I Fleisher, Intermetallic compounds, structural applications, John Willey & Sons IA 5001, USA (2000).

[16] Hong Fu et al., Recycling steel from grinding swarf, 1998.

[17] ASM handbook **Vol. 3**, Introduction to alloy phase diagrams, section 1.26.

[18] William D. Callister, Jr., Materials Sciences and Engineering an Introduction, 6th Ed. John, table 17.1, The Standard emf Series, Willey&Sons, Inc., 2003 USA.

[19] Hertzberg, Richard W. Deformation and Fracture Mechanics of Engineering Materials (4thEd.), 1995-12, Wiley.

[20] William D. Callister, Materials Sciences and Engineering, 7th Edition, John Wiley & Sons, 8th Ed., 2009, pp. 41, Atomic Radius Table 3.1.

[21] Grosselle F.et al., Correlation between microstructure and mechanical properties of Al-Si cast alloys, Metall Ital., **6** (2009), pp. 25-32.

[22] William D. Callister, Materials Science and Engineering: An Introduction 7th Ed., John Wiley 7sons, Inc., USA, 2007.

[23] ASM Handbooks **vol. 1 and 2**, Engineering materials Handbooks 1, 2 and 4, Metals Handbook: Properties and selection: Non ferrous alloys and pure Metals, **vol.2**, 9th a edition, and Advanced Materials & Processes, **Vol. 146,** No. 4, ASM International, Materials Park, OH, Modern Plastics Encyclopedia 1977-1978, The McGraw-Hill Companies, New York, NY; and manufacturers' technical data sheets.

[24] Fredriksson et al., Materials processing during casting, John Willey, 2006.

[25] Dutcher Daniel, Understanding rock candy fracture in steel castings, Ed. Modern Casting, February 1999.

[26] G.A Meerson and T. Segorheanu, The affinity of niobium for oxygen, Translated from Atomnaya, **vol. 16**, Dec 1962.

[27] William D. Callister, Materials Science and Engineering: An Introduction Seventh Edition, John Wiley & sons, Inc., Chap 4, USA, 2007, pp. 330-332.

[28] hhp://en.wikipedia.org/wiki/solid_solution_strengthening, retrieved June 13 2009.

[29] Edgar C. Bain, Functions of the Alloying Elements in steels, American Society for Metals, pp. 127.

[30] Handbook of Applied Engineering Science, Second Edition, 1973, CRC press.

[31] Kalpakjian, Manufacturing Engineering and Technology, **Vol. 11**, No. 7, pp.315-316. `

[32] Serope Kalpakjian et al., Manufacturing Engineering and Technology 5th Ed., Pearson Prentice Hall, pp.154-158.

[33] D.R. Gunasegaram et al., Melt characteristics and solidification growth direction with respect to gravity affecting the interfacial heat transfer coefficient of chill castings, Materials and Design (October 2009), **Vol 30** (9), pp. 35, Journal of Materials Processing Tech. (February 2009), pp. 1209-1219.

[34] Noé Cheunget al., Properties of spray-formed Fe–6.5%Si and Fe–6.5%Si–1.0%Al after rolling and heat treatment, Journal of Magnetism and Magnetic Materials (October 2008), **320** (20), pp. e653-e656.

[35] Claudemiro Bolfarini et al., Spray forming Magnetic property.

[36] Beckermann C, Viskanta R 1988 Double-diffusive convection during dendritic solidification of a binary mixture. Physico-Chem. Hydrodyn. **Vol 10**, pp.195-213, Beckermann C, Wang C Y 1995 Multi-phase scale modeling of transport phenomena in alloy solidification, In: Tien C L (ed.), Annual Review of Heat Transfer **Vol. 1**. Begell House, New York, pp. 115 - 98.

[37] P. Gilgen et al., Microstructure selection maps for Al-Fe alloys, « Département des matériaux, Ecole plytechnique de Lausanne », Switzerland Pergamo, Octobre 1994.

[38] http://corrosion.ksc.nasa.gov/galcorr.htm, Corrosion Technology laboratory, Galvanic corrosion, retrieved September 20, 2011.

[39] Timothy L., et al, Characterization and Correction of Casting Defects, Advanced Casting Technology, L.L.C.

[40] http://en.wikipedia.org/wiki/longitudinal_facial_crack#continuous_casting, Avedesian, Baker & ASM International (1999), Retrieved September 2011.

[41] Campbell, CASTING PRACTICE, The 10 rules of castings, ELSEVIER, Amsterdam, 2004.

[42] Serope kalpakjian et al., Manufacturing Engineering and Technology 5th Ed., Pearson Prentice Hall, pp. 262 - 272.

[43] William D. Callister and David G. Utah and Iowa Universities, Materials Science and Engineering: An Introduction e-copy 7th Ed, John Wiley & sons, Inc., USA, 2007, pp. 432.

[44] Zinn, Elements of Induction Heating, Design, Control, and Applications, pp.14.

[45] Jean Callebaut, Laborelec, Induction Heating, Section Energy efficiency, Power quality and utilization guide, Leonardo Energy February 2007, www.leonardo-energy.org.

[46] Zinn, Elements of Induction Heating Design, Control, and Applications, EPRI Electric Power Research, Institute Inc., pp. 7.

[47] Zinn, Elements of Induction Heating Design, Control, and Applications, EPRI Electric Power Research, Institute, Inc., pp.18 - 23.

[48] G. Krauss, Steels: Heat treatment and Processing Principles, ASM International, 1990, pp.108.

[49] Serope Kalpakjian et al., Manufacturing Engineering and Technology 5th Ed, Pearson Prentice Hall, Steven R. Schmid.

[50] Mohit Dhiman et al., Materials and Manufacturing Processes, **vol. 23**, pp. 805-808, India, 8 October 2008.

[51] Metals Handbook: Properties and Selection: Irons and Steels, **Vol. 1**, 9th edition, B. Bardes (Editor), American Society for Metals, 1978, pp. 36, pp. 461.

[52] Users guide of the Induction Power Supplies 3kW; 135-400 kHz, Tucker Induction Systems, Inc.50550 Rizzo Drive.

[53] MATWEB Material property data 2010, Overview of materials for AISI 100 series, Overview of materials for 6000 series alloy.

[54] ASM, Metals Handbook 9th Edition, **vol. 9** Metallography and Microstructures, aluminum alloys microstructures, USA 1985, pp. 366 - 388; pp. 230 - 236.

[55] ALCOA, Understanding extruded aluminum alloy, Engineered products, alloy 6061.

[56] Jean Callebaut, Laborelec, Induction Heating, Leonardo Energy, February 2007.

[57] hhp://en.wikipedia.org/wiki_Diamagnetism, retrieved July 20th, 2011.

[58] EUT researchers Jiri Cervenka and Kees Flipse, together with RUN colleague Mikhail Katsnelson, Eindhobren University of Technology (EUT) Randbon University Nijmeezen (RUN), Ferromagnetic properties discovered in graphite, Neetherland 2009, Softpedia Reviews Oct 5th, 2009.

[59] An educational, Fair Use website Electrical, NDT, Resistivity of Carbon, Graphite. The Physics Fact book, Edited by Glenn Elert.

[60] Zinn, Elements of Induction Heating Design, Control, and Applications, EPRI Electric Power Research, Institute, Inc2, pp. 24-25.

[61] Sonntag et al., Fundamentals of thermodynamics, Sixth Edition, Wiley, USA, 2003.

[62] www.engineeringtoolbox.com/fusion heat -metals-d_1266html, Metals and Latent heat of fusion.